UiT The Arctic University of Norway

Faculty of Science and Technology

Department of Physics and Technology

Antarctic ice shelf response to ocean tides and atmospheric pressure variations using satellite interferometry

An insight into Fimbulisen's vertical movements

Anna Odh

EOM-3901 Master's thesis in Energy, climate and environment 30 SP — June 2024

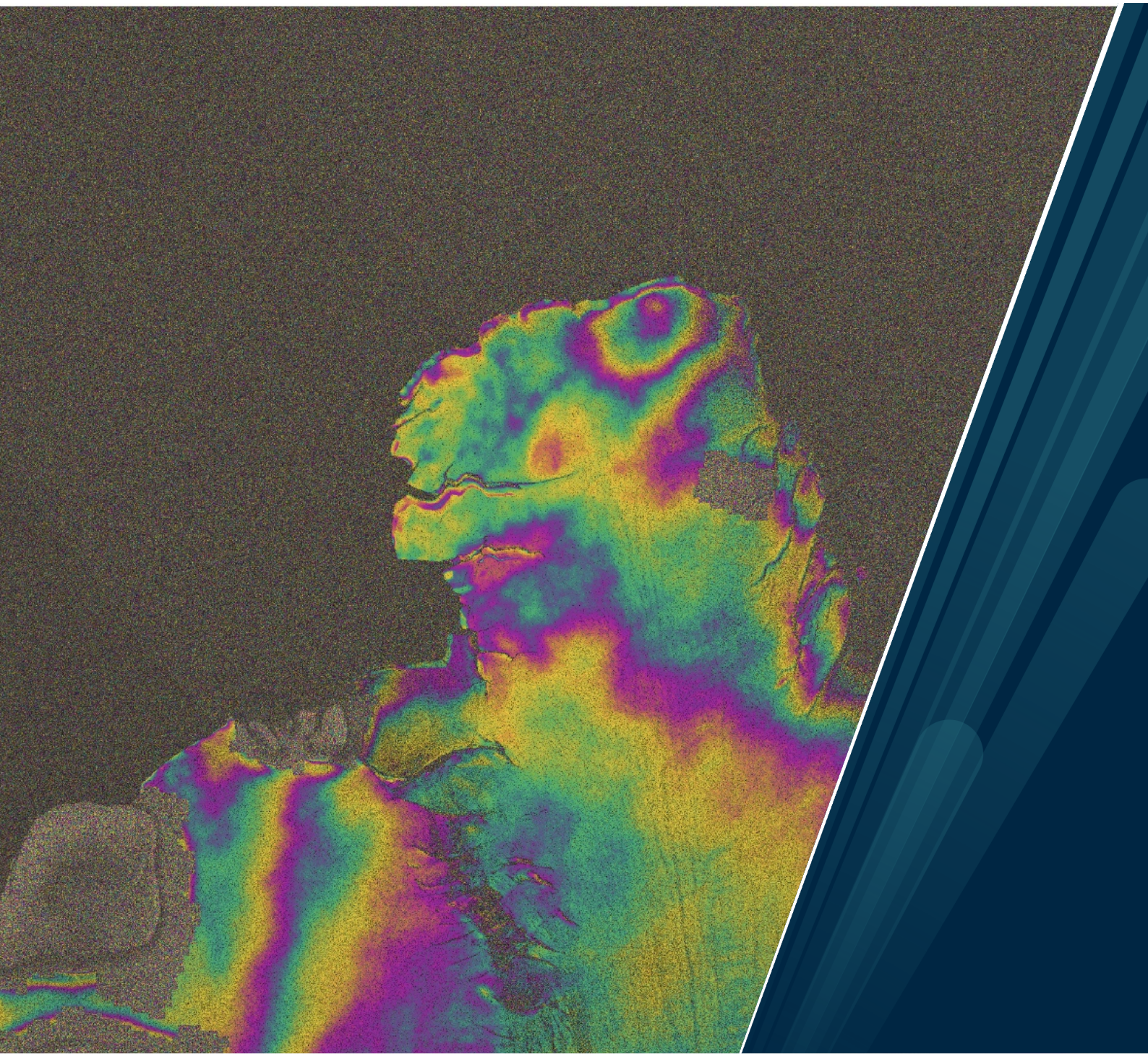

Abstract

Ice shelves, the floating extensions of the Antarctic ice sheet, are supporting the upstream ice and regulates the outflow into the ocean. They are a key component in future predictions of sea level rise, as their direct contact with both the ocean and the atmosphere makes them subject to changing climatic conditions.

This thesis aims to investigate how Fimbulisen, a large ice shelf in East Antarctica, responds to oceanic and atmospheric forcing through the use of satellite images in addition to tidal- and atmospheric pressure model data. As ice shelves float on the ocean, processes that make the sea level fluctuate, like oceanic tides and variations in atmospheric pressure, will affect their vertical movements. The vertical movement of an ice shelf can be analysed on the cm-scale with a satellite remote sensing technique called Triple- and Quadruple differential interferometry (T/Q-DInSAR). The T/Q-DInSAR imagery used in this thesis is derived from large swath (400 km) Synthetic Aperture Radar (SAR) imagery, covering the whole ice shelf of Fimbulisen.

In addition, an Antarctic regional tide model, CATS2008a, and a global atmospheric pressure model, ECMWF ERA5 reanalysis, are used in this thesis. Output from these models is processed to fit the interferometric epochs, shape and extent of the T/Q-DInSAR images, and subsequently, their effects on vertical movement are subtracted from the T/Q-DInSAR images. The remaining effects after subtraction, are assumed to tie to either inaccuracies in the tide- or atmospheric pressure models, or to other significant geophysical processes affecting the vertical movement of Fimbulisen.

The results show that the combination of the two models can resolve vertical movement adequately in well-known, freely floating cavities of ice shelves. The models do not resolve areas with ice rises and rumples well, probably due to ice flexure not being captured by the models. Trolltunga, a part of Fimbulisen overhanging the continental shelf break, is exposed to the Southern Ocean and displays displacement signals from several possible oceanic processes. A link between circular imprints in the T/Q-DInSAR data and warm deep water carrying ocean eddies was explored, through the use of in situ temperature mooring data from Fimbulisen. The imprints align somewhat with the theory on the eddies, both in size and timing. However, future work is needed and includes analysing the T/Q-DInSAR data with circular imprints through different T/Q combinations and extending the dataset over several years. Additionally, the appearance in the data needs to be tied to further theory on these types of eddies, like their expected surface expression.

Acknowledgements

I would like to express my deepest gratitude to my supervisors, Malin Johansson and Jelte van Oostveen. Your knowledge, great support and encouragement have inspired me from the start. Without it, this thesis would not have been possible. Thank you for teaching me about story-telling and how to think with the pen, and enabling such a cool project.

Acknowledgements go to the European Union Earth observation program Copernicus, for the use of Sentinel-1 data from 2019. Sentinel-1 data can be downloaded from https://scihub.copernicus.eu.

Interferometric data processing is carried out by NORCE using in-house developed and licensed software packages GSAR and GDAR.

The tide model data was provided from the CATS2008a-model [1], an update to the model by Padman et. al. (2002) [2]. The data was accessed using the pyTMD toolbox [3].

ERA5 hourly data on single levels from 1940 to present by Hersbach, H. et al., (2018) [4] was downloaded from the Copernicus Climate Change Service (2023) [5]. The results contain modified Copernicus Climate Change Service information 2020. Neither the European Commission nor ECMWF is responsible for any use that may be made of the Copernicus information or data it contains.

I would like to thank the people who have supported me throughout this thesis and my school years. To my partner Nils Liljeström; thank you for being the best mental support I could think of, without having any idea of what this thesis regards. The times climbing together and the dinners you made me, always made me wonder: how did I land you? To Karolina Haraldsson; thank you for being the best classmate, mountain partner and friend. The years in Tromsø would not have been the same without you. To my family; Olli, Rebecca, Karin and Hans-Anders. Thank you for supporting me no matter what, even if I move 2000 km away from Skåne. Being able to come home like I never left, to discuss horses and listen to live musical performances in the kitchen, has been invaluable.

Anna Odh

Tromsø, June 2024

Contents

List of Tables

List of Figures

Chapter 1

Introduction

In this chapter, the context and motivation of this thesis will be introduced in section 1.1. Section 1.2 presents the aim and objectives of this thesis. Finally, section 1.3 lays out the thesis structure.

1.1 Context and motivation

The global mean sea level rise is accelerating [6], threatening vulnerable coastal areas and communities globally [7]. Human-induced climate forcing is the main cause of global mean sea level rise since 1970, and the largest contribution is coming from the world's glaciers and ice sheets [8].

The Antarctic ice sheet contains an amount of ice mass that, if melted, would raise the global sea level by approximately 58 m [9]. The Antarctic ice sheet as a whole is experiencing ice mass loss at increasing rates [10], and is a definite contributor to sea level rise in future scenarios [11]. However, there is large uncertainty of its exact contribution [12].

Antarctica is divided into East and West Antarctica, and West Antarctica has been the dominating region for mass loss [13], and has been extensively researched. However, East Antarctica holds considerable more ice mass than West Antarctica, and has more recently been shown as a potential major contributor of Antarctic mass loss [14].

Antarctica is a key component in the climate system [15], facilitating a complex system of interactions between bedrock, ice, ocean and atmosphere. Ice shelves, the floating extensions of the ice sheet, surround 75% of the Antarctic ice sheet. Ice shelves play a crucial role in supporting the upstream ice sheet, and regulate its outflow into the ocean [16]. Thinning of ice shelves through basal melt is today the largest ablation process in Antarctica [17], and ablation of ice shelves can induce an acceleration of the outflow from the upstream ice sheet [18]. This makes ice shelves a crucial component to study in the prediction of sea level rise.

Through their direct contact with the ocean underneath and the atmosphere above, ice shelves are subject to oceanic- and atmospheric processes and changes. Ice shelves experience vertical movement from the processes affecting the sea surface height, where the oceanic tide cycle and atmospheric pressure variations have large influence of this movement over short time scales. Ice shelves can rise and fall up to several meters in synchrony with the tides [19], and an atmospheric pressure anomaly of -1 hPa can be approximated to induce a lift of 1 cm [20]. As the vertical movement of an ice shelf is linked to atmospheric and oceanic processes in this way, it is beneficial to study, to learn about how they react to their surroundings.

Ice shelf motion due to atmospheric pressure can be approximated over ice shelf areas with weather data containing atmospheric pressure, i.e. from the accessible global ERA5 reanalysis database [5][4]. For oceanic tide induced motion, Antarctic regional tide models like CATS2008a [2], are constructed to predict tides under ice shelves and around the coastlines of Antarctica. Regional tide models are widely used for ice shelf study in Antarctica, both for looking at ice shelf response to tides [19], but also to correct for tidal "noise" in satellite remote sensing data over ice shelves [21]. Antarctic regional tide models are however suffering from significant uncertainty in ice shelf areas [22], and model developments are needed for improved accuracy in ice shelf studies.

The vertical movement of an ice shelf can be monitored from space with a technique called triple/quadruple differential interferometry (T/Q-DInSAR). This technique utilizes the phase component from three or four repeat Synthetic Aperture Radar (SAR) acquisitions, to derive relative height differences between acquisitions, within a few cm. The resulting image connects to ice shelf vertical movement between acquisitions, over large areas (>100 km) with high spatial resolution (<100 m) [23]. The Sentinel-1 SAR mission's Extra Wide mode (areal coverage of 400 km) [24], is especially suitable for processing T/Q-DInSAR imagery covering the entirety of a large ice shelf in East Antarctica called Fimbulisen.

This leads to the **research question** of this thesis: Can the tidal model CATS2008a and atmospheric pressure data from ERA5 explain all vertical displacement signals in the T/Q-DInSAR imagery over Fimbulisen?

The **hypothesis** is that the CATS2008a and ERA5 datasets can explain all vertical displacement signals in the T/Q-DInSAR imagery.

1.2 Aim and objectives

This thesis' **aim** is to investigate Fimbulisen's response to oceanic/atmospheric forcing by using Triple/Quadruple-DInSAR.

The following **objectives** of this thesis are:

- Investigate ice shelf behavior by employing an ocean tidal model and atmospheric pressure data on T/Q-DInSAR time series
- Uncover ongoing processes affecting the motion of Fimbulisen
- Investigate how T/Q-DInSAR can be used to highlight flaws in tidal models
- Compare the T/Q-DInSAR imagery to in-situ data to explore the possibility of ocean eddies affecting vertical motion of Fimbulisen

1.3 Structure of thesis

Chapter 2 introduces the basic principles of Synthetic Aperture Radar, SAR Interferometry and Triple/Quadruple differential Interferometry.

Chapter 3 contains relevant background for this thesis: Antarctic glaciological concepts, the study area of Fimbulisen, tidal prediction and relevant previous work.

Chapter 4 introduces the three datasets used in this methods of this thesis: NORCE T/Q-DInSAR data, tidal data from CATS2008a and atmospheric pressure data from ERA5. Also, the mooring temperature data used for further analysis of the results is introduced.

Chapter 5 presents the methods used in this thesis.

Chapter 6 contains the results and discussion.

Chapter 7 presents the conclusions of this thesis along with future work.

Chapter 2

SAR theory

This chapter will present the basic principles of Synthetic Aperture Radar (SAR) in section 2.2, SAR Interferometry (InSAR) in section 2.3 and Triple/Quadruple differential InSAR (T/Q-DInSAR) in section 2.4. Firstly, the basic concept of imaging radar remote sensing will be introduced in section 2.1.

2.1 Basic concept of imaging radar remote sensing

Remote sensing is the process of acquiring information of a subject from afar. This can be done by mounting a sensor on for example drones, air crafts or satellites that will fly over Earth. If the sensors are imaging radar sensors, they are transmitting and receiving electromagnetic energy (EM) by the area they are monitoring. An EM wave can be described by the expression:

$$E = Ae^{i(kr-\omega t+\Phi)} = Ae^{i\phi} \tag{2.1}$$

where E is the electric vector, A is the amplitude, k is the wave vector in the medium that the wave propagates (dependent on the wavelength of the wave λ and the relative permittivity ϵ_r, see [25]), r is the position vector, ω is the angular frequency, t is the time and Φ is the phase [25]. The expression $(kr - \omega t + \Phi)$ is often simplified to being denoted ϕ, and called the *phase of the wave*. This phase is connected to a 2π change every time the wave travels a distance of its own wavelength [25].

Remote sensing instruments utilizes different parameters of the expression in 2.1 [25]. For this thesis, the important parameter is the phase of the wave ϕ, which can be used to detect ground movement on the mm-cm scale with interferometric SAR [26] explained in section 2.3

2.2 Synthetic Aperture Radar (SAR)

A SAR-sensor is transmitting electromagnetic waves towards the surface of the Earth, and registers the signal that is reflected back. The fact that it is both transmitting and receiving EM radiation implies that it an *active* satellite system. To be able to separate the signals received back from near-range (ground close to sensor) and far-range (ground far away from sensor), the sensor is side-looking. The so called satellite line of sight (LOS), what the sensor "sees", will therefore be at an angle towards the ground. Figure 2.1 is showing and explaining the SAR platform geometry.

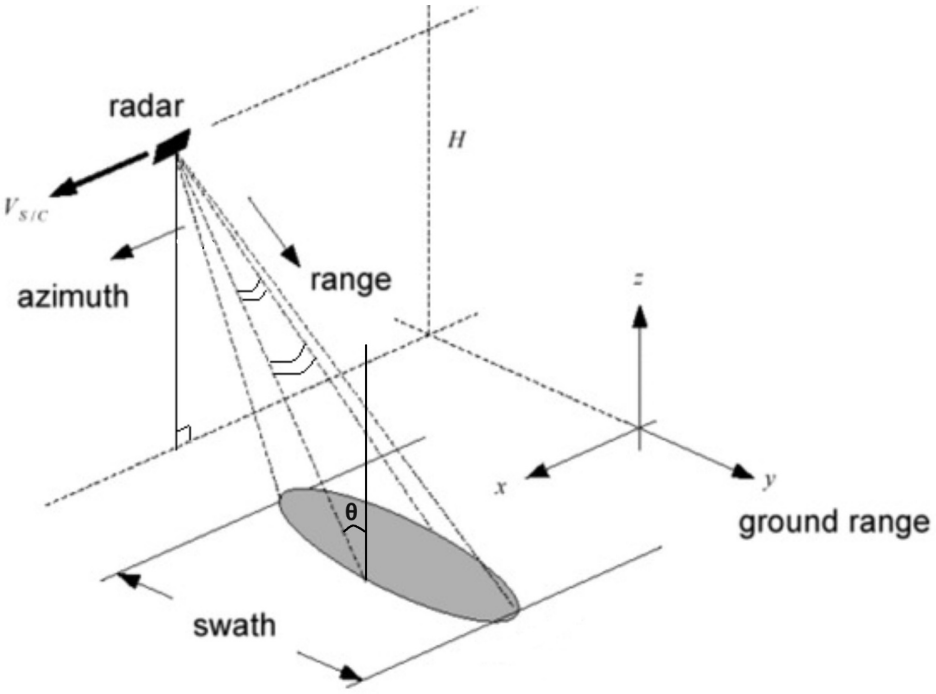

Figure 2.1: Geometry of a SAR platform. The sensor is moving with high velocity along its track (azimuth direction), and sending and receiving pulses in the line of sight across its track (range direction). The ground range is the range direction projected onto the Earth geoid. The swath is representing the size of the ground image. The incidence angle θ is the angle between the vertical direction and the radar beam; being lowest in the near-range and highest in the far-range. The platform's altitude H depends on its orbit, and is for example for the SAR mission Sentinel-1 around 700km [27]. Velocities of the platform are typically around 7km/second [28]. Modified from [29].

The EM wavelengths typically utilized by SAR sensors are on the centimeter scale - within the microwave part of the EM spectrum, see Figure 2.2. These wavelengths have the benefit of being able to penetrate through the atmosphere, so that a SAR sensor can deliver weather- and daylight independent monitoring. The most common SAR-bands can be found in Table 2.1.

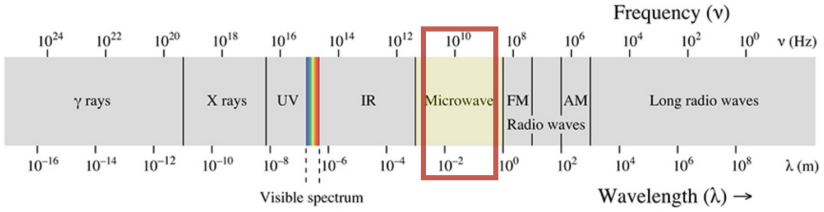

Figure 2.2: The electromagnetic spectrum. SAR wavelengths are marked within the microwave part of the spectrum. Modified from [30].

Table 2.1: Common SAR-bands with their wavelength and frequency.

SAR-band	Wavelength	Frequency
Ka	1.1–0.8 cm	27–40 GHz
Ku	2.4–1.7 cm	12–18 GHz
X	3.8–2.4 cm	8–12 GHz
C	7.5–3.8 cm	4–8 GHz
L	30-15 cm	1–2 GHz
P	100–30 cm	0.3–1 GHz

The SAR platform is flying over the Earth with a speed typically around $\sim$7.5 km/second [28]. A SAR sensor is utilizing this velocity by simulating a longer antenna, by combining several acquisitions from the real antenna [31]. By doing this, the spatial resolution achieved by a SAR sensor can be increased, meaning that the ground pixel size can become smaller.

The spatial resolution of a SAR sensor depends on several components in the SAR system. The ground range resolution X_r, which is the minimum distance at which two points on the ground can be separated in the ground range direction, is given by:

$$X_r = \frac{c}{2Bsin(\theta)} \tag{2.2}$$

where c is the speed of light, B is the bandwidth of the transmitted signal (equal to the spread of frequencies Δf) and θ is the incidence angle [32]. The ground range resolution is typically in the range of a few tens of meters.

The azimuth resolution X_a for a SAR system, that is, the minimum distance at which two points can be separated in the azimuth direction, is given by:

$$X_a = \frac{L}{2} \tag{2.3}$$

where L is the length of the antenna [33]. This is usually in the range of 10m. More details on SAR processing and principles can be found in SAR handbooks like in [31].

SAR satellite constellations can be launched into space on different orbits. For this thesis, it is relevant to introduce the sun-synchronous polar orbit. A polar orbit is where the satellite is going from pole to pole ("ascending" towards the north, "descending" towards the south) at a slight angle, as the earth is rotating under its track. If it is also in a sun-synchronous orbit, the satellite repeats its track over an exact area with the same light conditions, ie at the same relative position with the sun [34]. Sentinel-1A/B is an example of a sun-synchronous polar orbiting SAR satellite mission, which originally had two polar orbiting satellites with a repeat cycle of 6 days [24]. Repeat cycle refers to the time it takes for the satellite between two overpasses of the same area with the same conditions (i.e. viewing angle and relative position to the sun). The satellite repeat cycle is an important parameter in differential interferometric SAR, as it becomes the temporal baseline, see 2.3.

SAR processing will result in an image of complex pixels: a 2D array of rows and columns, often a single look complex image (SLC). Each pixel is a "resolution cell", and represents an area of the ground with one complex number, containing an amplitude and a phase [26]. The amplitude of a SAR image is showing the strength of the back scattered radar signal from the ground elements, and the phase is showing a delay connected to the travel time to the ground and back [35]. The SAR products of amplitude and phase images is represented in Figure 2.3. A phase image is not containing any useful information on its own, though when paired with other phase images over the same area that the phase information can prove useful - applied in interferometric SAR.

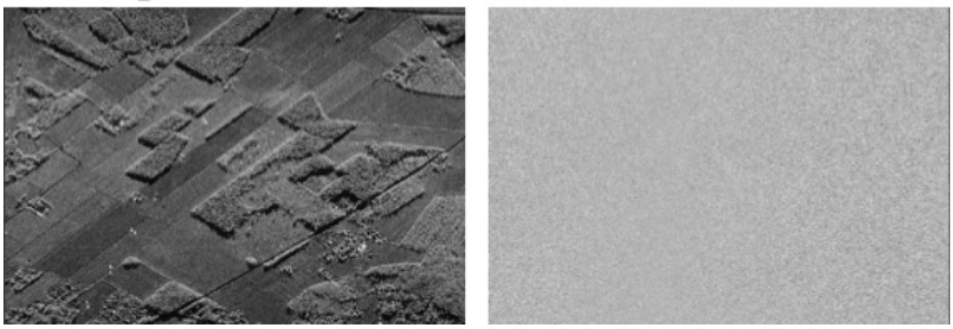

Figure 2.3: The product of SAR processing. Left: amplitude image. Right: phase image. Modified from [36].

2.3 SAR Interferometry

SAR interferometry is a processing technique which finds the phase difference between two SAR acquisitions to retrieve information about the ground surface. Before differencing, the two SAR acquisitions must first be aligned in space, with a processing step called co-registration [37]. This is done by matching each ground target to the same range-azimuth pixel in the two images [26]. After co-registration, an interferogram can be produced. This is done by multiplying the first complex SAR image with the complex conjugate of the second, pixel by pixel [26]. The equation below describes the operation to generate a complex interferogram image, I_{ifgm}:

$$I_{ifgm} = \mathbf{I_1} \cdot \overline{\mathbf{I_2}} = \mathbf{A_1} e^{i\phi_1} \cdot \mathbf{A_2} e^{i(-\phi_2)} \tag{2.4}$$

where $\mathbf{I_1}$ is SAR image 1 and $\overline{\mathbf{I_2}}$ is the complex conjugate of SAR image 2. The right-hand product represents the images in complex polar form with an amplitude and a phase component. This operation performs multiplication of the amplitudes of the images, and subtracts the phase of the second image from the phase of the first image.

What this phase difference can say about the ground surface depends on the interferometric baseline. The interferometric baseline is the difference in time or space (or both) between the SAR acquisitions [38]. If a difference in space is used as interferometric baseline, through different look angles of the ground, the terrain altitude can be derived [26]. For this thesis, InSAR using temporal baselines, meaning a difference in time between individual SAR acquisitions, will be utilized. This type of InSAR is sometimes called differential InSAR. Figure 2.4 is showing a representation of an InSAR with a temporal baseline. The time interval between the timestamps of acquisitions is called an epoch.

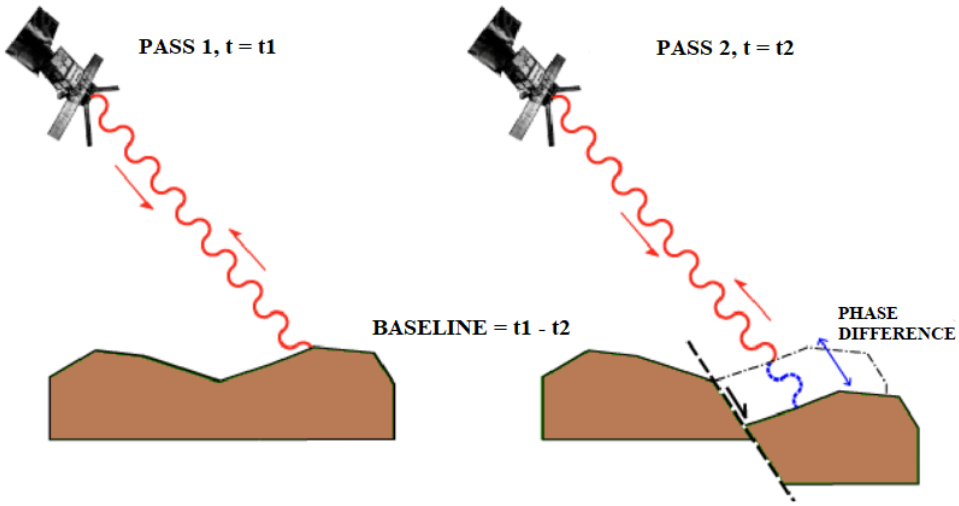

Figure 2.4: A representation of the InSAR principle with a temporal baseline. The baseline is the difference in time of pass 1 (at time t1) and pass 2 (at time t2), which can induce a phase difference if we have ground movement in between the passes. Modified from [39].

As seen in Figure 2.4, if there is ground movement between the two satellite overpasses, it will induce a difference in travel distance of the electromagnetic wave, which results in a phase difference, $\Delta\phi$, between acquisitions. The phase difference registered will be in the direction of LOS, containing both horizontal and vertical components.

To retrieve the phase of the complex interferogram, $\Delta\phi$, one finds the angle in the complex plane:

$$\Delta\phi = arctan\left(\frac{imag(I_1 \cdot \overline{I_2})}{real(I_1 \cdot \overline{I_2})}\right) \tag{2.5}$$

$\Delta\phi$ holds the total phase difference of the interferogram. The phase difference due to displacements in the LOS, $\Delta\phi_{LOS}$, will be embedded in this total phase shift, since there are other components contributing to the phase shift between two SAR acquisitions:

$$\Delta\phi = \Delta\phi_{LOS} + \Delta\phi_{atm} + \Delta\phi_{topography} + \Delta\phi_{flatearth} + \Delta\phi_{noise} \tag{2.6}$$

where $\Delta\phi_{atm}$ is the phase difference induced by atmospheric variations, $\Delta\phi_{topography}$ is the topography induced phase difference, $\Delta\phi_{flatearth}$ is the phase difference caused by the curvature of the Earth, slightly changing with the range distances across the image, and $\Delta\phi_{noise}$ is the term for phase noise [23]. The flat earth contribution can be corrected for, as it has a nearly linear phase change across the image [23]. The topographic effect can be removed by using a digital elevation model (DEM), however this model might carry some uncertainty which can not fully be accounted for. The phase noise can for example be caused by a change in the ground surface physical properties (i.e. how the ground scatters the transmitted signal) in the epoch [26], or a low signal to noise ratio (SNR) in the sensor signal. If the phase noise together with the atmospheric variations can be assumed negligible, the remaining signal is the most interesting one: $\Delta\phi_{LOS}$.

Together with the phase difference from an interferogram, it is possible to generate a phase difference quality measure, called coherence, for that interferogram. Coherence is a value between 0 and 1, where 0 means no valuable phase information due to noise, and 1 means no noise in the phase parameter [26]. How coherence is generated can be found in [40].

The interferogram phase image will be assigned a cyclic color code and become "fringed" over areas with phase differences. Each fringe represents a phase shift of 2π, or multiples of 2π, since the signal is periodic in nature. A LOS displacement of precisely half the radar wavelength, $\frac{\lambda}{2}$, will induce a 2π phase shift, or 1 fringe, in the interferogram [26]. Any multiplies of this LOS displacement will induce the exact same phase shift, so the interferogram phase can be ambiguous. The relationship between the LOS phase shift $\Delta\phi_{LOS}$ and the LOS displacement d_{LOS} is described with the equation below [26]:

$$\Delta\phi_{LOS} = \frac{4\pi \cdot d_{LOS}}{\lambda} \tag{2.7}$$

A representation of the InSAR principle can be found in Figure 2.5. For example, for a radar wavelength of 5 cm, one fringe would represent a LOS displacement of 2.5 cm, given no phase ambiguities. Since the LOS displacement can contain both horizontal and vertical components, differential InSAR alone is not sufficient to be able to retrieve only the vertical component of ground subsidence or uplift. A further technique, called double differential InSAR or Triple/Quadruple differential InSAR, can be utilized for this cause under certain conditions, explained in the next section.

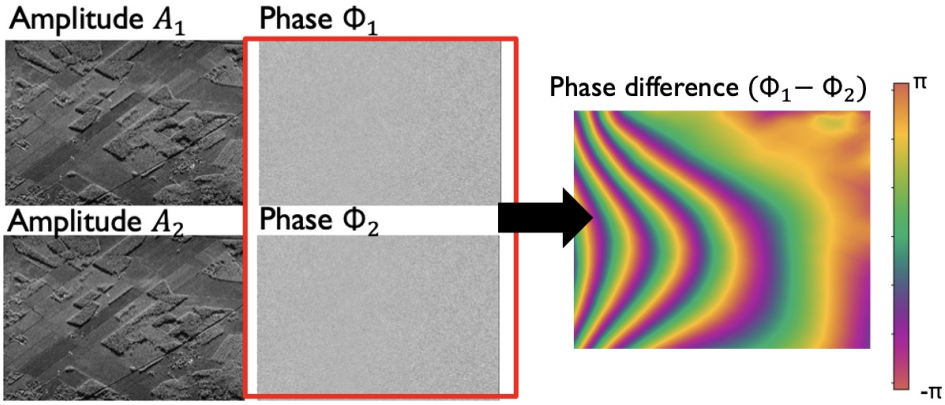

Figure 2.5: The principle of InSAR. The phase images from two SAR acquisitions are differenced to derive a fringed interferogram representing the phase difference between acquisitions. Modified from [36].

2.4 Triple/Quadruple differential interferometry

Triple/Quadruple differential interferometry, here denoted T/Q-DInSAR, is a processing technique which finds the phase difference between two interferograms. The two interferograms must have the same

temporal baseline (for example 6 days from Sentinel-1A/B overpasses), and are generated from SAR images from the same orbital track [23].

The T/Q-DInSAR interferograms can be generated from three (Triple DInSAR) or four (Quadruple DInSAR) phase images:

$$TDInSAR = (\phi_1 - \phi_2) - (\phi_2 - \phi_3) = \phi_1 - 2\phi_2 + \phi_3 \tag{2.8}$$

$$QDInSAR = (\phi_1 - \phi_2) - (\phi_3 - \phi_4) = \phi_1 - \phi_2 - \phi_3 + \phi_4 \tag{2.9}$$

where ϕ_{1-4} are the phase images from the four different SAR acquisitions. After making necessary corrections for non-negligible terms in the total phase difference (see equation 2.6), the remaining LOS phase difference for the triple- or quadruple combinations will be retrieved. The triple combination will extend over two connected interferogram epochs, and will take the second phase image into account twice, meaning this phase image has a larger impact on the resulting phase difference. The quadruple combination will use two interferogram epochs separated by a certain time, but will take each phase image into account only once.

For LOS phase change, the T/Q-DInSAR operation will cancel out all phase change that is the same in both interferograms; meaning where the ground movement has been equal in the two interferogram epochs. Applied to ice shelves (see a description of ice shelves in Chapter 3.1), if we assume completely constant horizontal movement/ice flow, T/Q-DInSAR will show the **remaining non-steady vertical movement** (projected onto the LOS) [23]. The possible reasons for ice shelves having vertical movement and why it is important to monitor is explained in Chapter 3.1.2. The assumption of steady horizontal movement might not be the case in reality, but the possible remaining horizontal term is in this application assumed much smaller than the vertical. The basic principle of double DInSAR (Quadruple case) is shown in Figure 2.6.

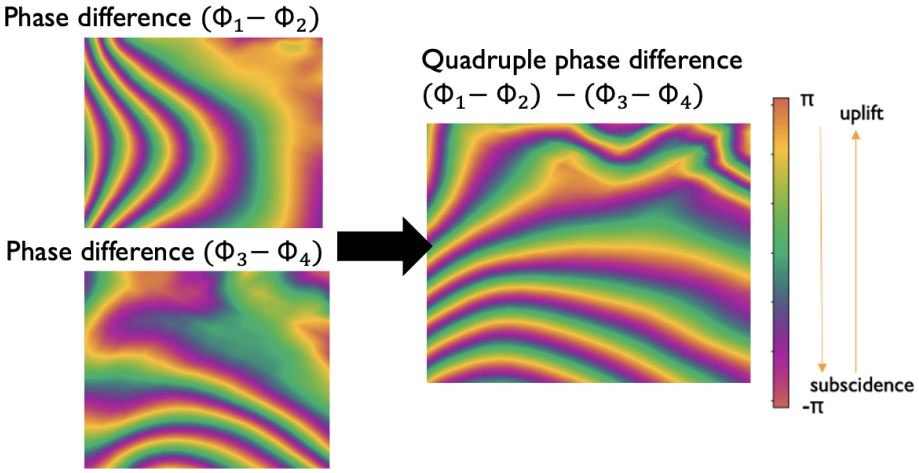

Figure 2.6: The basic principle of DInSAR, here showing a Quadruple difference. Two phase differences are differenced, and if the scene is over areas with constant horizontal movement, the remaining phase signal is only connected to vertical non-steady movement (projected onto LOS). The arrows indicating uplift and subsidence refers to *relative* uplift and subsidence in the T/Q-DInSAR combination.

Chapter 3

Background

This chapter will introduce the basic glaciological concepts of the Antarctic ice sheet and its ice shelves, some of their trends in a warming climate, and the study area of this thesis, the Fimbul ice shelf in section section 3.1. Oceanic tides and some of their effects on the Antarctic sheet and shelves will be introduced, as well as tidal prediction in Antarctica in section 3.2. Finally, relevant previous work using InSAR over ice shelves will be presented in section 3.3.

3.1 The Antarctic ice sheet and its ice shelves

An ice sheet is a mass of glacial ice covering an area over 50,000 km^2. The Antarctic ice sheet contains a mass of ice which, if melted, would rise global mean sea levels by around 58 meters [9]. The ice sheet is up to 4.9km thick at its center, where there is accumulation of snow [41]. This gives the Antarctic ice sheet a cone-like shape, as it presses out under its own weight, and triggers an ice flow out towards the ocean. Closer to the coast the ice flow becomes faster and can reach speeds of a few kilometers per year [42].

The fast-flowing ice can create an outlet glacier, which drains the upstream ice by an ice flow towards the ocean, often through a valley of mountains, or an ice stream. An ice stream is a longer section of fast flowing ice pressing through areas with much slower moving ice [41]. The main mass loss (called ablation) from the ice sheet happens in the coastal areas of Antarctica. These areas consists of: ice tongues; which terminate by slowly becoming thinner, ice cliffs; an abrupt edge down into the ground, ocean or surrounding sea ice, and ice shelves; bodies of ice still attached to the ice sheet, which have flowed over into the ocean and become fully afloat [43]. Ice shelves are supporting the upstream ice sheet masses and control the outflow of flow ice into the ocean. Ice rises and ice rumples are small sections of grounded parts in ice shelves, which provide a further stabilizing effect on the upstream ice [44]. See Figure 3.2 for a representation of these structures. See a representation of the Antarctic ice shelves and their supporting "qualities" (buttressing) in Figure 3.1. This thesis will focus on ice shelves in particular.

3.1.1 Antarctica in a warming climate

As a whole, the Antarctic ice sheet is losing mass at increasing rates [10], and is estimated to have contributed to sea level rise by 14.0$\pm$2.0 mm in the period 1979-2017 [14]. These mass losses are regionally varying in Antarctica, due to diverse ocean parameters like seawater temperature, sea ice formation and bathymetry (ocean floor topography), to mention a few [17]. Antarctica is a complex system of parameters interacting with each other: bedrock, ice, ocean, and atmosphere [47]. Future climate projections show that there is uncertainty regarding Antarctica's exact contribution to sea level rise through its mass loss [12].

Antarctica is divided into East and West Antarctica, split by the Trans-Antarctic mountains. West Antarctica has been the dominating region when it comes to mass loss, and it was previously thought that the East Antarctic sector was not experiencing any significant mass loss, and even gaining mass [13].

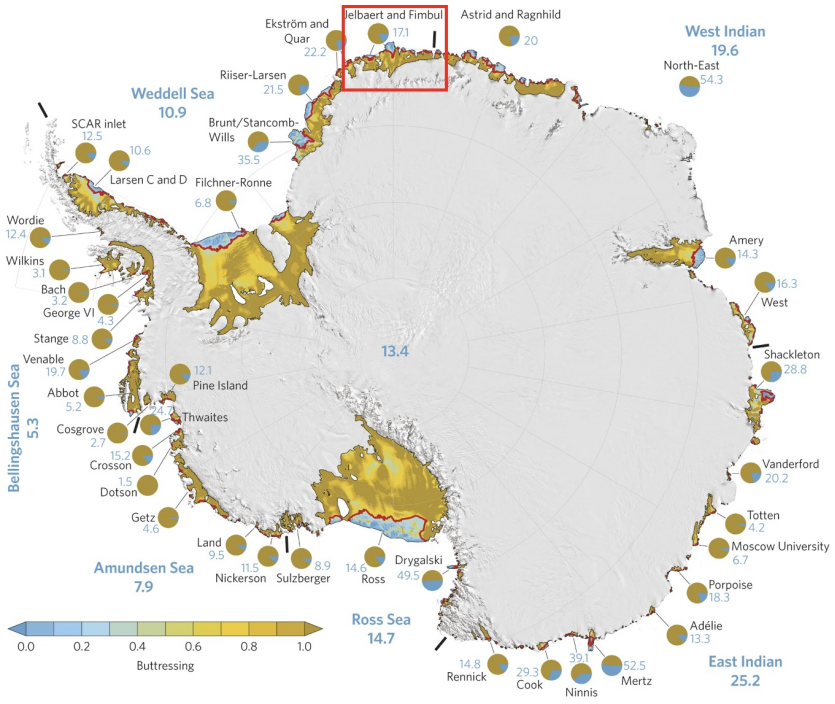

Figure 3.1: The Antarctic ice shelves and their buttressing (see [16]). The area of Fimbulisen is marked in red. Modified from [16].

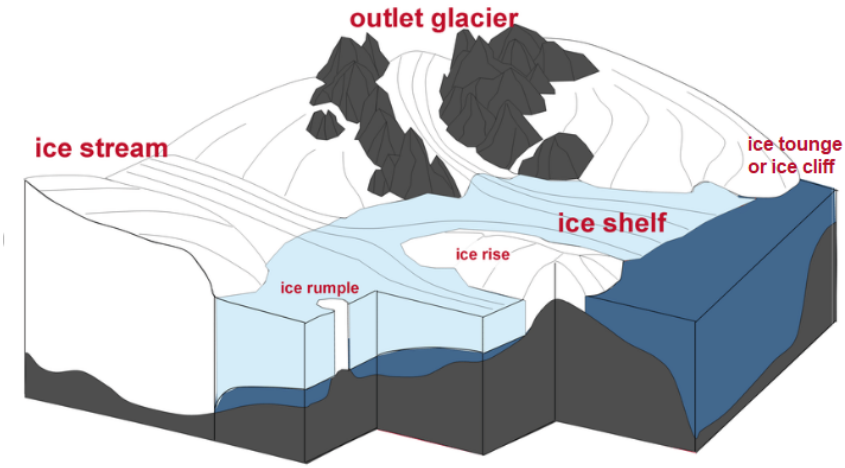

Figure 3.2: A 3D representation of the glaciological components of the Antarctic boundaries. Ice rises are rising above the ice shelf surface and ice rumples are features below the ice shelf. Modified from [45], courtesy of Angelica Humbert after [46].

However, more recent evidence has shown that East Antarctica, which is storing 90% of all the Earth's ice mass, has in fact been a major contributor of the mass loss in the period 1979-2017 [14].

3.1.2 Ice shelves and grounding zones

Ice shelves can extend from the ice sheet into the ocean for tens to hundreds of kilometers, and are up to 600 meters thick [48]. They are responsible for Antarctica's main ablation processes [17], which happens through calving and basal melting. Calving is when icebergs break off at the outer edge of an ice shelf, and basal melt occurs when the underside of the ice shelves melt due to warm ocean temperatures. A more dramatic event of ablation can also happen through ice shelf disintegration, which is when an ice shelf breaks apart on a larger scale than that of a single calving event [49].

Ice shelves are an important component when predicting Antarctica's mass loss, since ice shelf ablation is contributing indirectly to sea level rise, as their stabilizing effect on the upstream ice sheet can be significantly reduced because of ice shelf thinning or disintegration [16]. This leads to an acceleration of outflow from the upstream ice sheet, which adds to sea level rise [50]. As ice shelves have contact with both the atmosphere and ocean, they are sensitive to changes is air- and ocean temperature [51]. Rignot et. al. (2013) estimated that basal melt of ice shelves is the number one ablation process of Antarctica, rather than iceberg calving as previously thought [17]. Further, melt water from ice shelves was estimated by Rignot et. al. (2013) to be around 28% too high to keep Antarctica's ice shelves in an "overall steady state", in the period of 2003-2008 [17]. It has also been shown that thinning was occurring at higher rates in the period 2003-2012 compared with that of 1993-2003 [52].

The position where the ice shelf comes in contact with the ocean and lifts off the underlying bed is called the grounding line. The grounding line is located within the grounding zone, which is a wider area where the ice goes from being fully grounded to fully afloat, see Figure 3.3. As ice shelves float on the ocean, they are affected by processes that make the sea level fluctuate. The largest contributor to this process is the ocean tide, however other geophysical factors can also have a significant effects on sea level height, see section 3.2.2. For the fully freely floating part of an ice shelf, seaward of "H" in Figure 3.3, these effects will make an ice shelf rise and fall vertically in synchrony with the oscillation of sea level, essentially without delay [19]. However, in the grounding zone, the ocean processes can cause the ice to bend due to its elastic material properties, even inland of the grounding line until the limit of tidal flexure, "F" in Figure 3.3[53]. An ice shelf can also experience flexure close to where it might be locally grounded by ice rises or rumples.

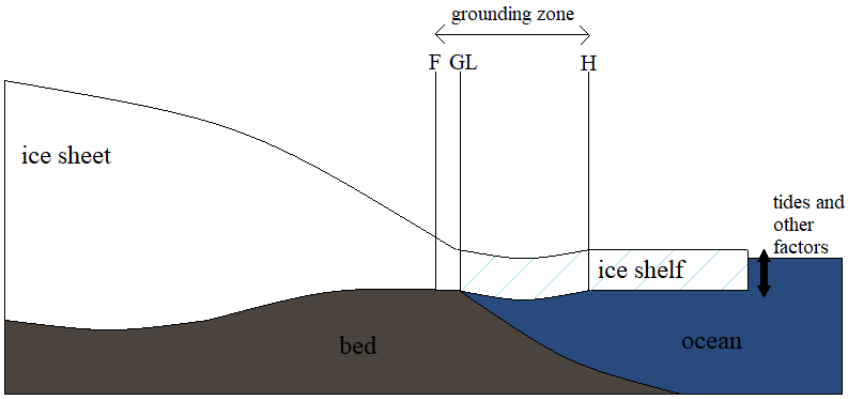

Figure 3.3: A 2D representation over the ice sheet-ice shelf transition (after [54] and [53]. The grounding zone spans over the grounding line (GL) from the inward limit of tidal flexure (F) to the seaward limit of ice flexure (H).

The grounding line position has been recognized as an essential climate variable (ECV); a variable that "critically contributes to the characterization of Earth' s climate" [55]. Since the main mass output from the ice sheet flows over the grounding line, its position is important for mass-budget calculations [56]. Further, grounding line retreat is an indicator of sea level rise or thinning of ice shelves [57], since a lift of the ice shelf will move the grounding line inland.

3.1.3 Study area: Fimbulisen

The Fimbul ice shelf, or Fimbulisen, is located in Dronning Maud Land (DML) in East Antarctica. It is the sixth largest ice shelf in Antarctica, extending from around 69°S to 72°S and 3°W to 8°E, about 100 km wide and 200 km long. The Norwegian research station Troll is positioned 235 km inland, see Figure 3.4.

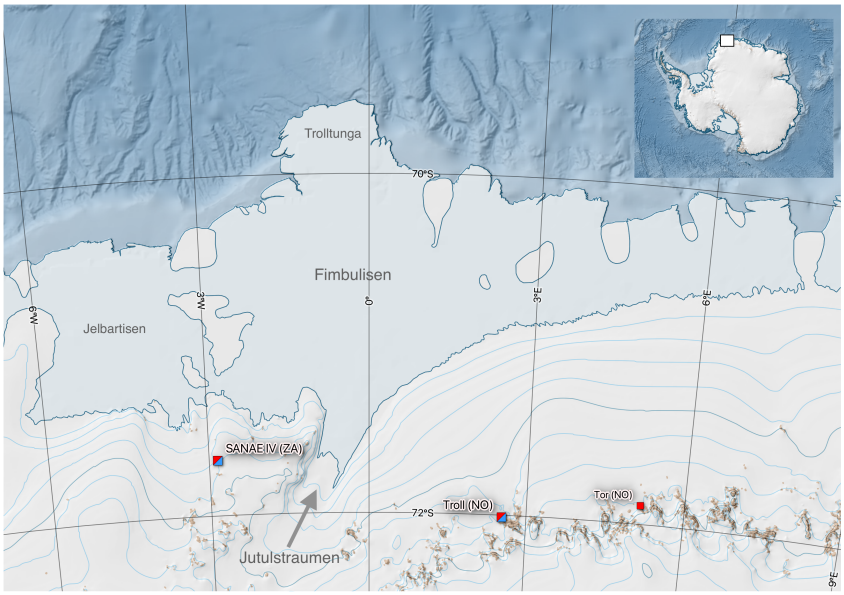

Figure 3.4: A map over Fimbulisen on the Antarctic Polar Stereographic projection EPSG:3031. Jutulstraumen ice stream and Trolltunga are marked, as well as the research stations in the area. Modified from the Norwegian Polar Institute's Quantarctica package, using the detailed basemap [58][59][60].

Fimbulisen has several ice rises and rumples, both on its east and west sides in Figure 3.4, which are stabilizing the ice shelf. Fimbulisen is fed with ice by the fast flowing Jutulstraumen, the largest ice stream in DML, draining an area of 124.000km^2, with a velocity of about 750 m/year [61], see Figure 3.5. The areas east- and west of Jutulstraumen consist of slower moving ice, which results in crevassing between these zones because of large differences in velocity [62]. Jutulstraumen flows northwards through the ice shelf out to Trolltunga, creating a ice tongue with a calving front out into the ocean.

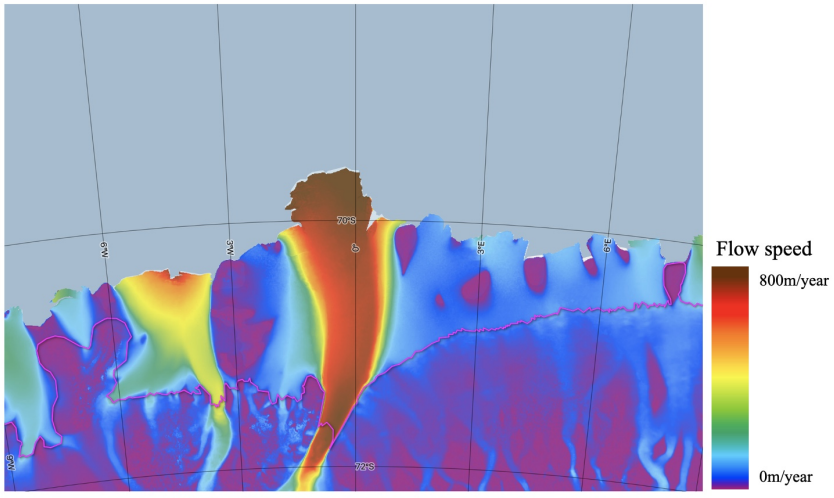

Figure 3.5: Flow speed map over Fimbulisen. Based on MEaSUREs flow speed, acknowledging [63] and [64]. The pink line indicates the grounding line derived from [65]. Modified from the Norwegian Polar Institute's Quantarctica package, using the simple basemap [66].

Through a seismic study conducted on Fimbulisen by Nøst et al. in 2004, the underlying bathymetry and water column thickness of the ice shelf became known, and Fimbulisen has one of the better known bathymetries in Antarctica [67]. The middle part of Jutulstraumen, often called the "central cavity" of Fimbulisen, has water column thicknesses of up to 900m. The outermost part of Trolltunga extends out over the continental shelf break, as it floats over depths of over 2000m, see Figure 3.6. The underlying bed of Fimbulisen can be characterized as a retrograde bed, meaning that the sub-glacial topography deepens inland.

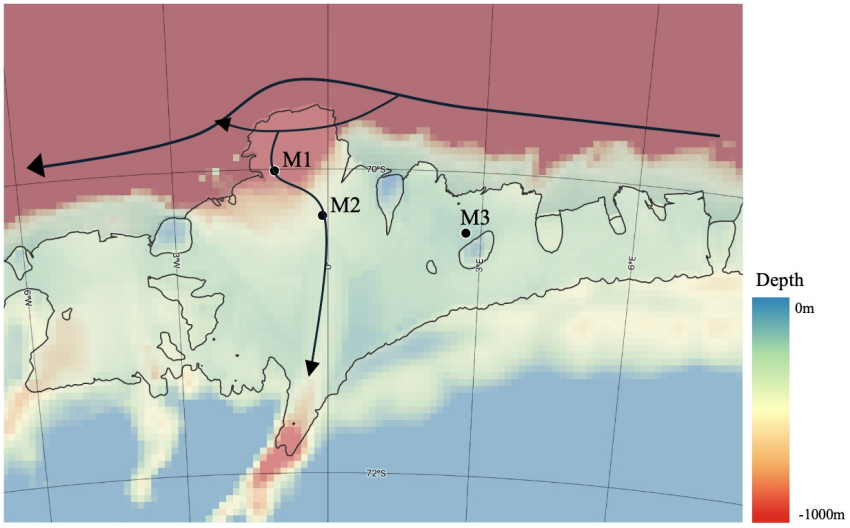

Figure 3.6: Bathymetry map over Fimbulisen, covering depths of 0 to -1000m, after Figure 1(a) in the study by Lauber et. al. (2024) [68]. The black dots indicate the approximate positions of the Norwegian Polar Institute's mooring stations M1, M2 and M3. The arrow going across the coast of Fimbulisen is representing the Antarctic Slope Current, with a possible passage underneath Fimbulisen. The downward arrow suggests the way of warm deep water through a "sill" into the central cavity. Bathymetry is based on data from 2010 published by Le Broq et. al. [69]. Coastlines are from Mouginot et. al (2017) [70]. Modified from the Norwegian Polar Institute's Quantarctica package [66].

Fimbulisen and the other ice shelves in DML are more protected from warm water intrusion than the West Antarctic ice shelves through the Antarctic slope front, which is separating cold and warm water masses in the ocean [71]. The slope front generates the Antarctic Slope Current [72], which flows to the west past Trolltunga, across the coast of DML.

However, warm water intrusion under Fimbulisen has more recently been to linked to diminishing sea ice cover and stronger sub-polar westerly winds [73]. Since 2016 there has been more frequent warm water intrusion below Fimbulisen, and an almost doubled mass loss rate through basal melt was found in the central part of the ice shelf [73]. Further evidence show that basal melt rate in the period of 2017-2021 of Fimbulisen was around 1 m/year, with variability seasonally but also sub-weekly, where higher ocean current velocities underneath the ice shelf induced peaks in melting [74].

To monitor the water temperature underneath Fimbulisen, three sub-ice shelf mooring stations were installed by the Norwegian Polar Institute in 2009, and were maintained until 2021. They provide temperature, pressure and velocity observations at the mooring sites M1, M2 and M3 (see locations in Figure 3.6). Through the observations, important insights about sub-ice shelf conditions of Fimbulisen have been gained. For example, warm deep water intrusion across a sill (a connection between the open ocean and the central cavity) in this period was observed by Lauber et. al. (2024) [68] under Fimbulisen. In the study, warm deep water intrusion was linked to the transport of cyclonic eddies (clockwise rotating in the Southern hemisphere) across the sill, which could reach all the way under the ice shelf to the grounding line. The cyclonic eddies in the study were estimated to have a mean radius of about 8 km. The warm water intrusion was linked to two periods in the year: January to March and September to November.

Mooring site M1 was located over the deepest part of the sill under Fimbulisen, and the deepest instrument of this mooring ($M1_{low}$, around 100m above the seafloor) is best suited for warm deep wa-

ter inflow observations [73]. Such observations have been connected to satellite derived basal melt of Fimbulisen [73]. The three moorings were renewed in the Antarctic summer of 2023-2024, as part of the Troll Observing Network (TONe) program [75].

3.2 Tides around Antarctica

The gravitational forces from the relative positions of the moon, earth and sun in combination with the earth's rotation are globally causing tides, making the sea level oscillate. The vertical changes around the mean sea level (MSL) are accompanied by horizontal tidal currents. The different components of the astronomical forcing are contributing to tides at different strengths and periodicity, and can be sorted into what is called tidal harmonic constituents. For example, M_2 is the strongest tidal harmonic constituent from the moon's gravitational force on Earth, and has a tidal period of 12.42 hours [76]. The tidal periods can be categorized as diurnal, with one high and low tide a day, semi-diurnal, with two high and low tides a day, or a mixture of both, with two uneven high and low tides a day. The tidal range - the difference in sea level between high and low tide - are around 1 to 2 meters on ice shelves in Antarctica, but some ice shelves experience up to 5 meters tidal range [2].

3.2.1 Tidal influence on Antarctic ice

The tides affect the Antarctic ice sheet and its ice shelves in several ways. Beyond the vertical rise and fall of freely floating ice shelves, the tides can change the grounding line location throughout their cycles [77]. During a high tide, the incoming ocean water can lift the ice shelf off its bed and make it afloat further inland, moving the grounding line several kilometers upstream [78, 77]. This phenomenon leads to temporally varying grounding of ice shelves, which can further induce a temporally varying ice flow speed and therefore upstream stability [79]. Tides can also cause the ice to bend in the grounding zone or close to ice rises and rumples, mentioned in section 3.1.2. Tides are also affecting a whole range of oceanic parameters that contribute to mass balance of the ice shelf through its underside, like circulation and heat-exchange between the water and ice, in addition to variation in velocity and frictional forces underneath the ice shelf, to mention a few [19].

Given the influence of tides outlined above it is important to model them correctly to estimate: i) the effect tides has on the ice sheet mass balance parameters in order to accurately predict future mass balance estimations [23], but also ii) the "noise" introduced by the tides in satellite measurements to estimate the long term signals in the area [19]. Tides are referred to as noise in long term signals, since they have a large impact on the MSL (cm-m-scale) over short time scales, and other smaller signals (mm-scale) in satellite data will be masked by the tidal signals. Accurate removal of tides through tide models are therefor necessary. Noise removal of the tides is for example needed for long term estimates like ice shelf thickness change, i.e. made by Hogg et. al. (2021), using the tide model CATS2008a to extend the ice shelf thickness change record from 1992 to 2017 [21].

3.2.2 Tidal prediction over ice shelves

The astronomical forcing of tides are periodic in nature and provides a solid basis for tidal surface displacement prediction. Most tidal models, global and regional, are barotropic, meaning that they assume currents to be constant with water depth [19]. The largest limitation of tidal model accuracy is the estimation of water column thickness; meaning the water depth in open waters and under ice shelves. There are several regional tide models developed specifically for the ocean around Antarctica and its ice shelves (see for example [22]). These models are resolving coastal features around Antarctica better than the coarser global tide models [19]. In [22] five regional tide models for Antarctica were compared (including the tide model used in this thesis - CATS2008a). The comparison concluded that the tidal height output in the open ocean for the five models had differences of less than 5cm. The largest disagreements were found around the coastlines of Antarctica, where model output could defer from each other with up to 60cm [22].

Hence, tidal modelling around the Antarctic coastline is more challenging than for the open ocean. The estimation of water column thickness in these models depends on both accurate bathymetry and ice shelf thickness. In addition, the land-ocean transition must be resolved for both the coastline as well as the grounding line. Assimilated data is coming from for example satellite altimetry (measuring surface

height from space) and in-situ tide gauge records (continuous water level monitoring). The satellite altimetry measurements are challenged by their sparse coverage, and the harsh Antarctic climate means tide gauges are relatively few [22]. The deep cavities under ice shelves and in the open ocean off the coast suffer from sparse bathymetry sampling [80, 9], and the ice thickness estimates can have errors of order up to 100m [81].

The three main oceanic forcings on ice shelves, the parameters in "traditional tide modelling", is described by Wild (2018) [54] as:

- tidal harmonic constituents
- atmospheric pressure anomalies
- tidal load - the deformation of the Earth's surface because of the weight change due to the ocean tides

The contribution from the tidal load is relatively small compared to the tidal harmonic constituents and atmospheric pressure anomalies [82]. The atmospheric pressure is inducing change when it deviates from the mean atmospheric pressure, and adds a non-harmonic signal on similar timescales as the tides, which needs to be accurately accounted for. Atmospheric pressure anomalies can be estimated to induce a change of sea level according to the inverse barometric effect (IBE): 1cm change per opposite sign 1hPa anomaly [20].

Other effects, not considered in traditional tide modelling, are for example ocean eddies and sustained ocean waves, which can also have a considerable effect on these time scales [83]. Changes in river outflow into the ocean and changes in ocean density (driven by changes in salinity and temperature) can also be of significance [76].

3.3 Previous work using satellite interferometry to study tidal prediction over ice shelves

Significant previous work of using T/Q-DInSAR (see Chapter 2.4) to improve tidal prediction over ice shelves has been done in a PhD thesis by C. Wild published in 2018 [54]. In his work, traditional tide modelling output was improved by up to 74% in Antarctic coastal areas, by combining T/Q-DInSAR data with tide model output and GPS surface height measurements.

An article associated with this PhD thesis included an investigation of the tide model CATS2008a tidal height output against T/Q-DInSAR data [84]. GPS surface measurements were used to subtract the IBE in the T/Q-DInSAR data, and the residual height was compared to the tidal output over a freely floating area of an ice shelf. The mean difference estimate between the tide model and the T/Q-DInSAR data was 0.002 ± 0.086 m. The large standard deviation argued to be due to inefficiencies in CATS2008a when capturing tides under the ice shelf.

The PhD work in [54] concluded that there is need for further work of validating of tidal model output in more and in different types of grounding line areas. The work was made over a small ice shelf area called Southern McMurdo ice shelf, using a satellite mission with a swath width of about 40 km (TerraSAR X-band mission [85]). In this master thesis, a satellite mission with a swath width of 400 km covering the whole Fimbulisen ice shelf will be utilized, enabling more insights from combining tidal, atmospheric pressure and T/Q-DInSAR data over a larger area.

The pre-project of this master thesis was studying tidal- and atmospheric pressure T/Q interferograms together with T/Q-DInSAR imagery over Fimbulisen [86]. The tidal and atmospheric pressure difference interferograms were derived from three or four tidal- and atmospheric pressure snapshots. From the project paper, it was learned that T/Q-DInSAR imagery is a complex representation of several tidal- and atmospheric pressure stages in time. This is illustrated in Figure 3.7, where the tidal heights on a point outside the coast of Fimbulisen are overlaid with three example SAR acquisition times in Figure 3.7.

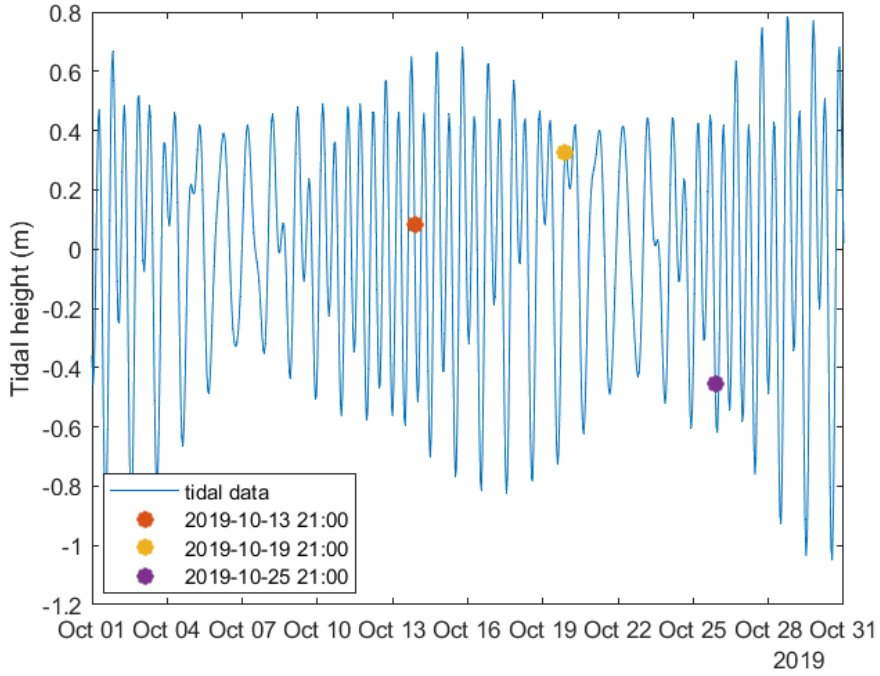

Figure 3.7: The tidal heights (from CATS2008a) in October 2019 on a geographical point just outside the coast of Fimbulisen (69.5°S, 0°W), and three acquisition times with 6 day revisit time. Figure from [86]

Chapter 4

Data

Three datasets are used for the main part of this thesis: a) NORCE T/Q-DInSAR data derived from Sentinel-1 Extra Wide (EW) raw data (see section 4.1), b) tidal data from the Antarctic model CATS2008a (see section 4.2), and c) ECMWF ERA5 reanalysis mean sea level pressure data (see section 4.3). The two latter datasets are open and freely available. An overview of the datasets' spatial and temporal resolution can be found in Table 4.1. An additional dataset is used for further analysis of the thesis results regarding a possible connection to ocean eddies: the sub-ice shelf temperature data from a mooring station at Fimbulisen, see section 4.4.

Table 4.1: The datasets with their spatial and temporal resolution. CATS2008a predicts tides from equations that will take in any temporal resolution.

Dataset	Temporal resolution	Spatial resolution
NORCE T/Q-DInSAR data	6 days	around 100 m x 100 m (depending on near/far-range)
CATS2008a tidal model	Anytime	4 km x 4 km grid
ECMWF ERA5 surface pressure data	1 hour	0.25°lat, 0.25°lon grid

4.1 T/Q-DInSAR data

The satellite constellation used for retrieving the SAR-data, Sentinel-1A/B (EW), is introduced. Then, the specifics of the NORCE T/Q-DInSAR data is explained.

4.1.1 Sentinel-1A/B (EW)

The Sentinel-1 (S1) mission consisted of two polar orbiting satellites; Sentinel-1A and Sentinel-1B, which together have a repeat cycle time of 6 days. The data used in this thesis is from when S1B was still operational, i.e. before December 2021. The onboard SAR-instrument on Sentinel-1 is a right looking C-band sensor with a centre frequency of 5.405 GHz, which corresponds to a wavelength of 5.547cm.

S1 has several acquisition modes with different swath widths and spatial resolutions, two of which will be discussed here. The standard acquisition mode is the interferometric wide swath mode (IW), which has a swath of 250km which it acquires in 3 sub-swaths, and has a spatial resolution of 5x20m [87]. Each sub-swath consists of bursts (short sequences where the antenna is swept over the target area), which are processed as single SLC images [88]. This provides an accurate alignment of small geographical areas (burst images) monitored over time. Overall, the IW mode provides a data product which is good for InSAR, also due to the baseline accuracy and the Doppler stability, see [87]. However, the IW mode does not provide imaging sufficiently covering Fimbulisen, so in this thesis, the S1 data used is acquired with the Extra Wide swath (EW) mode.

The EW swath acquisition of track 60 is covering the whole ice shelf of Fimbulisen in ascending pass. In comparison to the IW mode, the EW mode has a larger swath width of 400km, acquired in 5 sub-

swaths, and a lower spatial resolution of 20x40m [89]. Over the swath, the incidence angle range from 18.0°to 47°across the range. The EW mode has the **same suitability for InSAR** as the IW mode, but is currently not commonly used for interferometry. Figure 4.1 is displaying the areal coverage of the IW and EW mode.

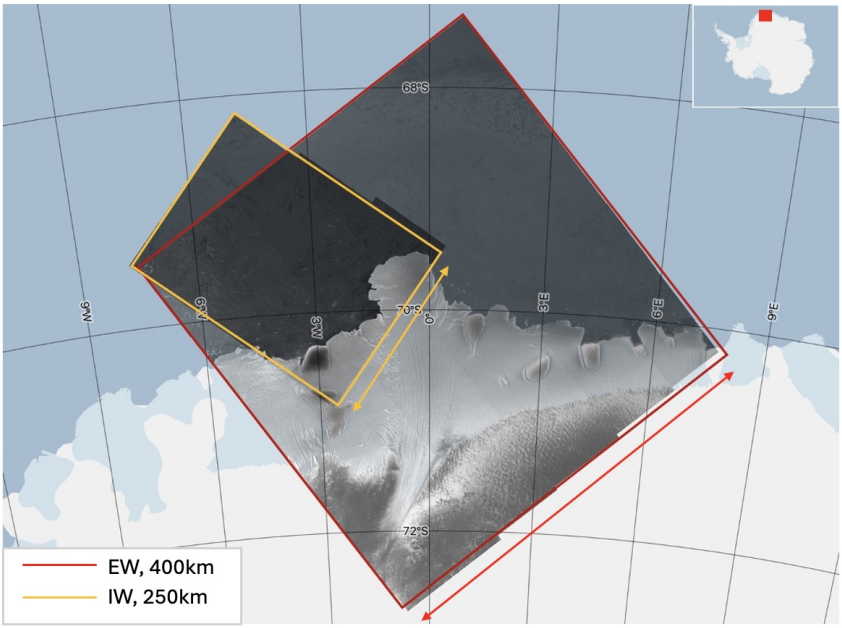

Figure 4.1: The approximate areal coverage of the S1 EW mode (track 60, red box) and the S1 IW mode (track 50, yellow box), visualized over the area of Fimbulisen. The EW mode covers the entire ice shelf of Fimbulisen. Modified from Copernicus Sentinel data [2024] [90] and displayed on a basemap (EPSG:3031) from the Norwegian Polar Institute's Quantarctica package [66].

4.1.2 NORCE T/Q-DInSAR data

The T/Q-DInSAR data used in this thesis is in-house processed by NORCE, from raw S1 EW SAR data to T/Q-DinSAR data. The single interferograms that the T/Q-DInSAR data is generated from is also provided by NORCE, here denoted InSAR data. The data is in satellite coordinates, range and azimuth, and each pixel carries a complex number.

The data processing is done through multiple steps. These steps will only be listed and not explained, and explanations of the steps can be found in InSAR processing handbooks like [91]:

- Raw format S1 data is focused and transformed to SLC format
- Co-registration of all bursts in the sub-swaths
- Flat-earth and topographic phase correction
- InSAR generation, burst-wise
- Multi-looking (a method to improve the radiometric resolution of the image, i.e. reducing SAR inherent speckle and therefore improving the signal to noise ratio (SNR). The image is multi-looked with 5 looks in range and 4 looks in azimuth
- Merging of bursts into a mosaic
- Phase filtering using a modified Goldstein filter
- T/Q-DInSAR generation using a minimum coherence calculation

The multi-looking operation reduces the spatial resolution to approximately 100x100m, depending on near/far-range (pixel sizing becomes larger in the far range to be able to keep the same SNR).

For this thesis, S1 acquisitions from the whole year of 2019 are used, see the acquisition timestamps in Appendix 8.1. Aside from 4 SAR acquisitions dates in May 2019 that are missing, the 6 day repeat cycle

is available throughout the year.

The geocoded interferometric phase of a NORCE T-DInSAR image can be found in Figure 4.2, showing the geographical extent of track 60.

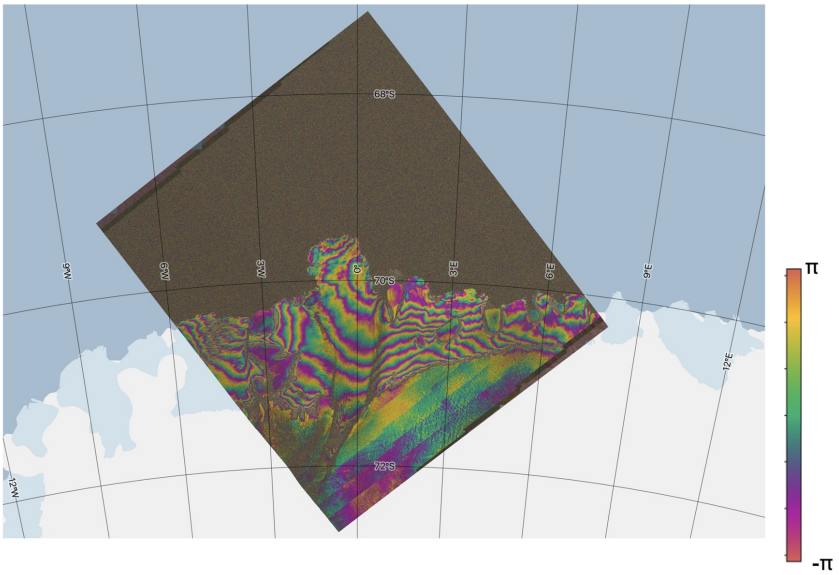

Figure 4.2: The interferometric phase from a NORCE processed Triple DInSAR image, based on Sentinel-1 acquisition dates 2019-02-15, 2019-02-21 and 2019-02-27 over track 60A. The image is geocoded and plotted over the interferometric coherence, on the basemap (EPSG:3031) from the Norwegian Polar Institute's Quantarctica package [66].

4.2 CATS2008a tide model

The tide model used in this thesis is the Antarctic regional inverse tide model CATS2008a (Circum-Antarctic Tidal Simulation), an update to the model described by Padman et. al. (2002) [2]. It is a high resolution model on a 4km Antarctic Polar Stereographic grid, centered at 71°S, 70°W, and includes the 10 major tidal constituents over the open ocean and also under floating ice shelves. The model resolves coastlines by using feature detection data from optical MODIS images, and matches this data to grounding line detection data from altimetry and InSAR. The model assimilates data from different datasets; radar and laser altimetry data over sea-ice free open ocean and some ice shelves and a set of observational tide records from the Antarctic Tide Gauge Database [92].

The output used from the model is surface heights in meters, 'z'. The output is in this work retrieved using the python toolbox pyTMD, which can be accessed from [3]. There is also a corresponding Matlab toolbox, accessed from [93]. The tidal data used is retrieved over a geographical grid covering Fimbulisen, see Figure 4.3.

4.2.1 Known limitations of CATS2008a

CATS2008a has some known limitations which affect the output of surface height 'z', provided by [94]. Firstly, it does not provide the effect on surface height due to ocean tide loading (the adjustment of underlying seabed due to load). As mentioned in Chapter 3.2.2, the ocean tide load is one of the three components in traditional tidal modelling, but will not be included here. This could induce a systematic error in predicted tidal height, since tidal load can induce effects on the 10mm-scale around the Antarctic coast [95]. Secondly, the location of the grounding lines of the ice shelves are not fixed as it moves back and forth with the sea level, bu this is assumed by the model. Further, the tide model only produces valid output where we have freely floating ice, and close to grounding lines or where there is ice flexure, tidal heights are reduced. Over Fimbulisen, CATS2008a has an uncertainty estimation of 5-7cm [96].

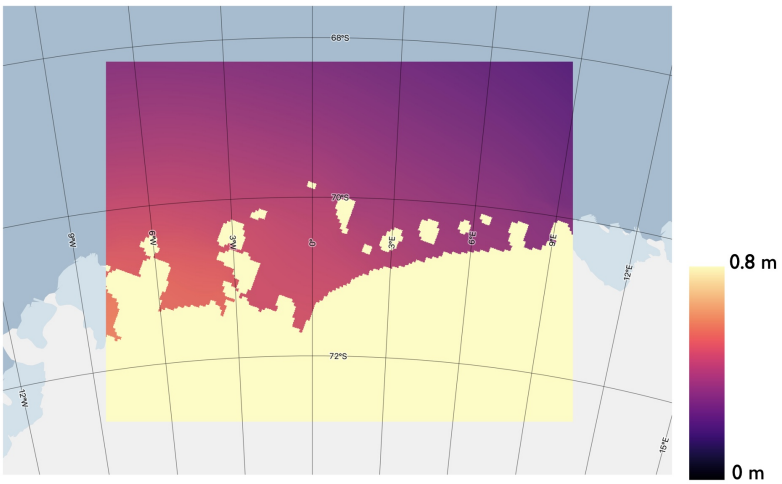

Figure 4.3: A tidal height output on 2019-03-11 20:24:29 UTC from CATS2008a over an area covering Fimbulisen. The basemap (EPSG:3031) is from the Norwegian Polar Institute's Quantarctica package [66].

4.3 ECMWF ERA5 atmospheric pressure data

ERA5 is reanalysis data improved from the ECMWF weather model [5][4]. "Reanalysis" is combining the prediction from a model with available observations to optimise the estimation for the parameters. ERA5 is providing an hourly output of atmospheric, oceanic and land parameters from 1940 and forward in time. The output is on a 0.25°latitude and 0.25°longitude grid.

Mean sea level pressure (mslp) is retrieved from the ECMWF ERA5 database[5][4]. Data from the database is downloaded on the two timestamps closest to the SAR acquisition time; at 20:00 and 21:00 UTC each 6 day repeat pass of year 2019. A surface pressure snapshot over Fimbulisen is shown in Figure 4.4.

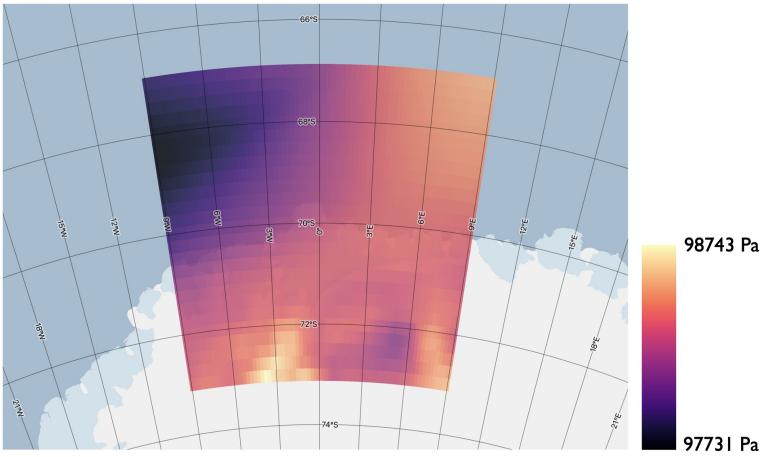

Figure 4.4: An ERA5 mean surface pressure output on 2019-03-11 20:00 UTC over an area covering Fimbulisen. The basemap (EPSG:4326) is from the Norwegian Polar Institute's Quantarctica package [66].

4.4 Mooring temperature data

Sub-ice shelf mooring ocean temperature data is used for further analysis of the resulting T/Q-DInSAR images retrieved from this thesis, see Chapter 6.4. The data is from mooring station M1; one of the three mooring stations maintained by the Norwegian Polar Institute on Fimbulisen, mentioned in Chapter 3.1.3. The M1 mooring station's geographical position was 1°E, 70 °S in 2009, and 1.1°E, 70 °S in

2022. The data used is from the deeper instrument, $M1_{low}$, located around 100m above the seafloor.

The data is accessed through the website Norwegian Polar Data Centre [97]. The output is daily average sub ice shelf temperatures, used from the whole year of 2019, see Figure 4.5.

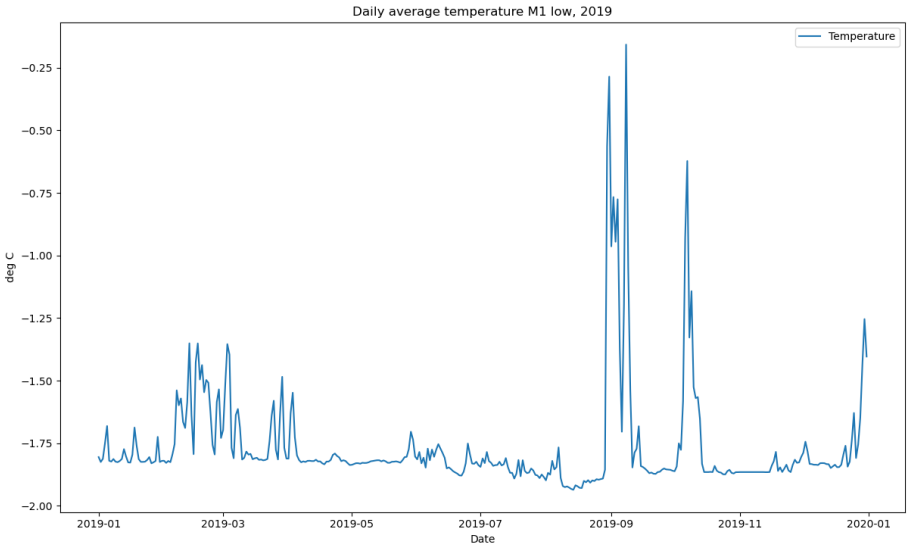

Figure 4.5: The daily average mooring temperatures of mooring station 1 (M1) in 2019.

Chapter 5

Methods

To study the influence of tides and atmospheric pressure on ice shelf behavior, these components should be subtracted from the T/Q-DInSAR data. The steps to do this are described in this chapter. First, in section 5.1, the generation of tidal- and mean sea level pressure (mslp) single snapshots from the tidal model CATS2008a and ERA5 reanalysis data is described. Second, in section 5.2, the methodology of generating single interferograms from these snapshots is laid out, including the processing needed to fit to the InSAR data. Third, in section 5.2, the generation of triple and quadruple difference interferograms and the subtraction of these from the T/Q-DInSAR images (here denoted just T/Q-DInSAR images) is described. Lastly, a method for analysing the results is explained in section 5.4.

The methods described in this chapter are based on a set of scripts, initially provided by NORCE, that form an extension of software suite GDAR, which is developed, owned and licensed by NORCE. Some scripts were adapted to suit the particular application of this thesis.

5.1 Generating tidal- and atmospheric pressure snapshots

This section explains how the single tidal- and mslp snapshots are retrieved, and Figure 5.1 is showing a representation of this process. The SAR acquisition timestamps are extracted from the metadata in the NORCE InSAR data (hereafter simply denoted InSAR data).

5.1.1 Retrieving tidal images from pyTMD

The tidal snapshots are calculated using the pyTMD toolbox [98]. First, a 2D grid covering Fimbulisen is created in the Antarctic polar stereographic coordinate system (EPSG:3031). The spacing on the grid is set to 1 km, while the model originally has a 4 km resolution, hence the tidal output data is spatially interpolated by the pyTMD functions. The tidal height, 'z', is retrieved on the grid for each SAR acquisition timestamp to generate tidal images. An example of a tidal image is shown in Figure 4.3.

5.1.2 Retrieving atmospheric pressure images from ERA5

The ERA5 mslp snapshots downloaded from the ECMWF ERA5 database (see Chapter 4.3) over a grid covering Fimbulisen, are linearly interpolated between the two closest points in time (20:00UTC and 21:00UTC) to fit each SAR acquisition timestamp. An example of such an interpolated image is shown in Figure 4.4 in Chapter 4.3. The mslp snapshots then are masked over the grounded ice with a mask over Fimbulisen.

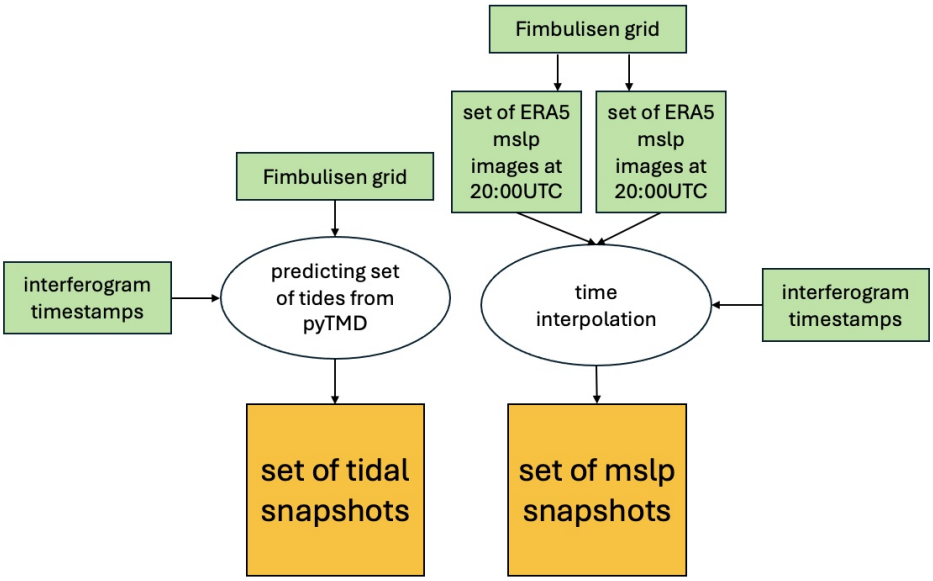

Figure 5.1: Flowchart representing the generation of mslp- and tidal snapshots. It is showing the input data (green boxes), processing steps (white ellipses) and output data (yellow boxes).

5.2 Generating tidal- & atmospheric pressure interferograms

This section explains how the tidal- and pressure data is processed to overlap the InSAR data in space and time. A representation of the processing steps explained in this section is found in Figure 5.2. The InSAR data provide the SAR acquisition timestamps in the metadata, and a digital elevation model (DEM) is used for back-geocoding (explained in section 5.2.2). Throughout the processing, a mosaic of the Reference Elevation Model of Antarctica (REMA) over Dronning Maud Land (100 m resolution, over-sampled from a 200 m product) is used [99]. The InSAR data is firstly cut to fit a down-sampling operation by a factor (10,10), to make the back-geocoding operation more efficient.

5.2.1 Finding tidal height- and atmospheric pressure differences

Firstly, the tidal height- and atmospheric pressure differences between the InSAR timestamps are found, through simple subtraction. For example, for the InSAR image generated from acquisition times 2019-01-04 20:25:13 and 2019-01-10 20:24:31, the corresponding tidal height difference image, z_{diff} between tidal height image on timestamp 1 (2019-01-04 20:25:13) z_1, and tidal height image on timestamp 2 (2019-01-10 20:24:31) z_2 would be found as:

$$z_{diff} = z_1 - z_2$$

The same is done for atmospheric pressure images. This is denoted "differencing" in the flowchart in Figure 5.2. From here on, further processing is made on these tidal- and atmospheric pressure differences.

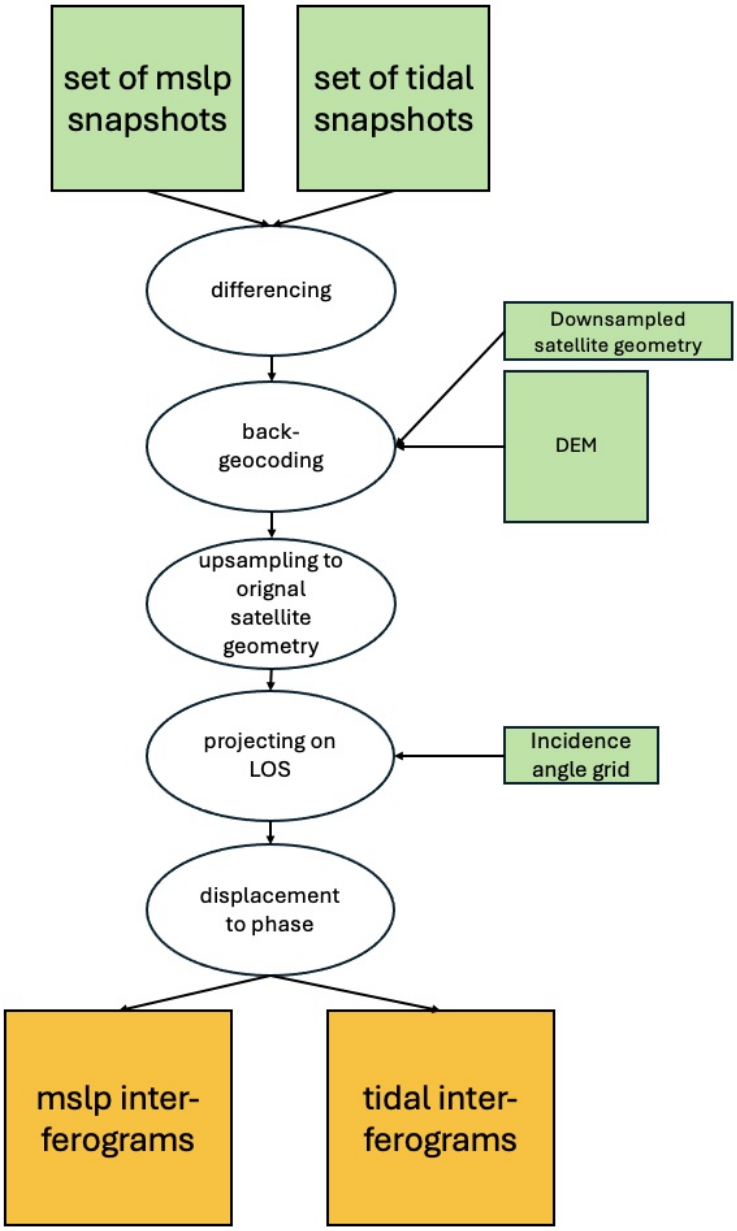

Figure 5.2: Flowchart representing the generation of mslp- and tidal interferograms. It is showing the input data (green boxes), processing steps (white ellipses) and output data (yellow boxes).

5.2.2 Back-geocoding

Geocoding of a SAR image refers to referencing each range-azimuth pixel to a coordinate in a geographic or projected coordinate reference system [100]. The coordinates of a map projection can be for example in latitude and longitude (geographic) or northing and easting (projected).

The opposite, called back-geocoding, refers to transforming an image from being in geographical coordinates, into satellite coordinates. A DEM is used in back-geocoding to adjust for the topography induced effects inherent to a SAR constellation (i.e. foreshortening, layover, shadowing), which will need to be induced in the tide- and mslp images also. Back-geocoding is performed on the tidal- and mslp images to fit the same geographical coordinates of the InSAR data. The tidal- and mslp images cover a different area than the satellite reference geometry of track 60A, see Figure 5.3, and only the overlapping part is back-geocoded and used further.

The InSAR satellite geometry is also used to get the tidal- and mslp images in the same spatial resolution and shape as the satellite imagery. In the back-geocoding operation, the tidal- and mslp snapshots

are therefore up-sampled to fit the size of the down-sampled InSAR image.

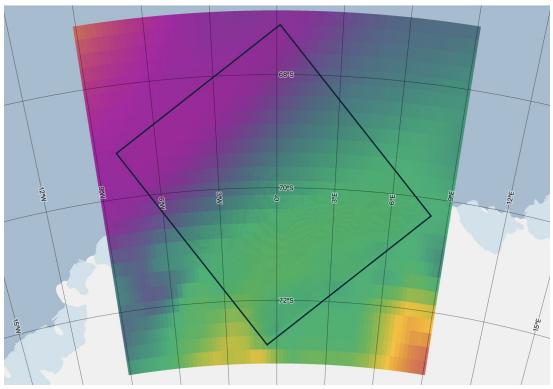

Figure 5.3: The geographical extent of the mslp images (color, here from 2019-08-20, 20:25:19) and the geographical extent of the satellite images (black rectangle) on EPSG:3031. The back-geocoding operation done is resampling the mslp- and tidal images to track 60, in azimuth-range coordinates. The basemap is from the Norwegian Polar Institute's Quantarctica package [66]

After back-geocoding, the mslp- and tidal images are upsampled a second time, this time by the down-sampling factor (10,10), to match the shape of the original InSAR image. The tide-, mslp- and InSAR images thereafter have the same shape and spatial resolution of the InSAR images (approx. 100x100 m pixel size). An example of the input and output when back-geocoding a mslp image is shown in Figure 5.4.

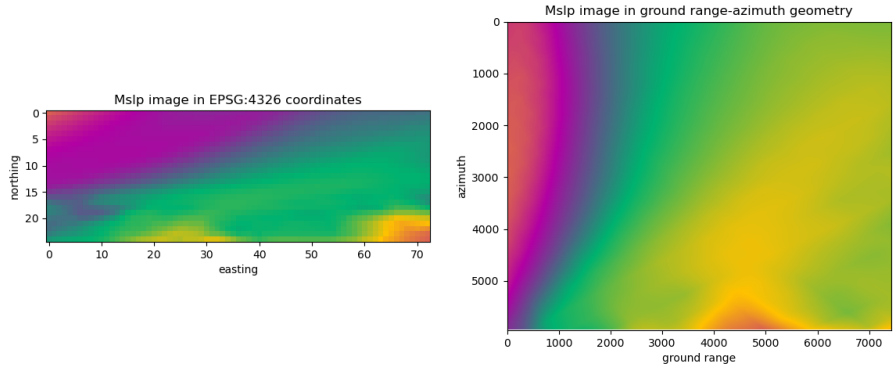

Figure 5.4: The input image (left) and output image (right) of up-sampling and back-geocoding of a mslp image (here a single snapshot from 2019-08-20, 20:25:19) to track 60A. The input image is a mslp image in the lat/lon coordinate system (EPSG:4326). The output image is the back-geocoded mslp image in SAR geometry over the extent of track 60A. Note that the left image (coloured area in Figure 5.3) covers a larger geographical area than the right image (black rectangle in 5.3).

5.2.3 Converting atmospheric pressure difference to displacement

An increased pressure at the ocean/ice shelf surface will press the surface down, and a decreased pressure will make the surface lift. The difference of two pressure images displays the pressure change between acquisitions, and will therefor be connected to a surface height change between acquisitions.

The surface height change can be approximated by the IBE: $+1hPa \rightarrow -1cm$ which is assumed to apply everywhere. The pressure difference is therefore multiplied by a factor of $-\frac{1}{10000}$, since:

$$+1hPa \rightarrow -1cm \leftrightarrow \tag{5.1}$$

$$+1Pa \rightarrow -0.0001m \tag{5.2}$$

5.2.4 Projecting vertical height on the LOS

The tidal and and mslp images show vertical displacement, and this is transformed into the corresponding satellite LOS geometry. Since it is assumed that the signals observed on the ice shelf primarily come from vertical movement in the T/Q-DInSAR image (see chapter 2.4), the vertical displacement is projected onto the direction of LOS and forms $proj_{L\vec{O}S}\vec{v}$:

$$proj_{L\vec{O}S}\vec{v} = \vec{v} \cdot cos(\theta) \tag{5.3}$$

Where $\vec{v}$ is the vertical vector with tides or mslp displacement, and θ is the SAR sensor incidence angle. See representation in Figure 5.5.

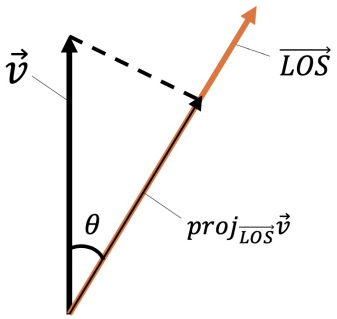

Figure 5.5: The projection of the vertical vector on the LOS.

The angle between the vertical and the LOS (incidence angle θ) is changing throughout the range of the satellite images, see figure 5.6 which is showing the incidence angle grid.

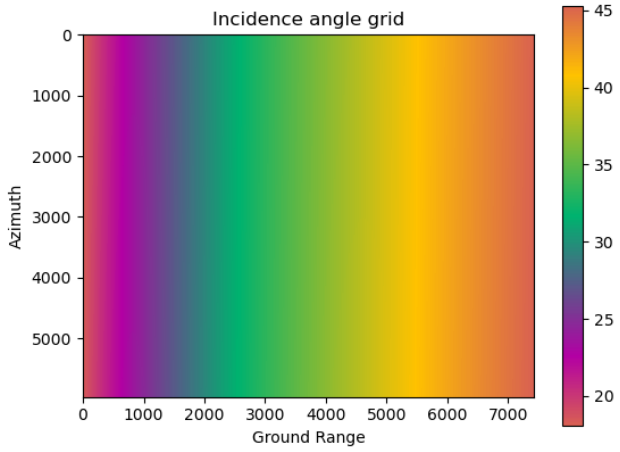

Figure 5.6: Incidence angle grid with a range from 18°to 47°indicated by the colorbar.

5.2.5 Converting displacement to phase

The LOS displacement is transformed into a complex image, $\mathbf{I_{complex}}$, with an amplitude of 1 and a phase transformed from the LOS induced displacement through equation 2.7:

$$\mathbf{I_{complex}} = e^{i \cdot d_{LOS} \cdot 4\pi/\lambda} \tag{5.4}$$

An example of the phase of such an image is shown together with its corresponding LOS displacement in Figure 5.7.

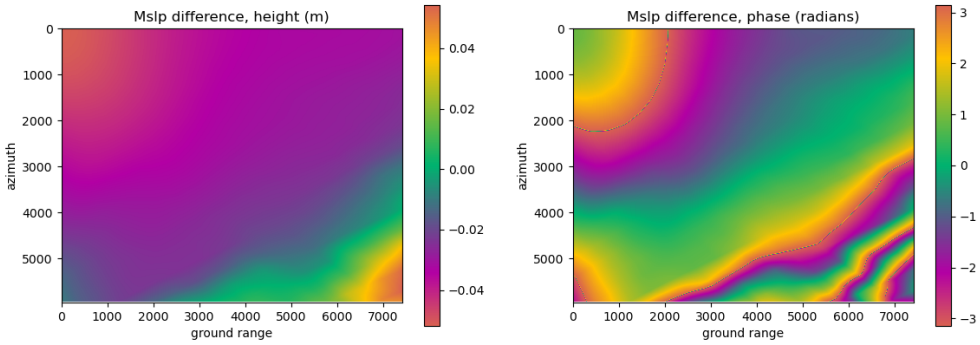

Figure 5.7: The mslp LOS displacement in meters (left) and the corresponding phase image in radians after the displacement-to-phase conversion (right).

5.3 Correcting the T/Q-DInSAR images for tides and atmospheric pressure

This section explains how the T/Q-DInSAR images are corrected for tides and atmospheric pressure. An example representation of this process, for a triple difference interferogram, is shown in Figure 5.8.

Firstly, tidal- and mslp triple and quadruple difference interferograms need to be generated from the tidal- and mslp interferograms. Since these are complex valued, this subtraction is done through multiplication of the complex conjugate. For example, to generate the tidal triple difference interferogram $I_{tide1223}$ from timestamps 2019-01-04 20:25:13, 2019-01-10 20:24:31 and 2019-01-16 20:25:12, tidal interferogram 1 I_{tide12} (generated from epoch 2019-01-04 20:25:13 - 2019-01-10 20:24:31), is multiplied with the complex conjugate of tidal interferogram 2 I_{tide23} (generated from epoch 2019-01-10 20:24:31 - 2019-01-16 20:25:12):

$$I_{tide1223} = I_{tide12} \cdot \overline{I_{tide23}}$$

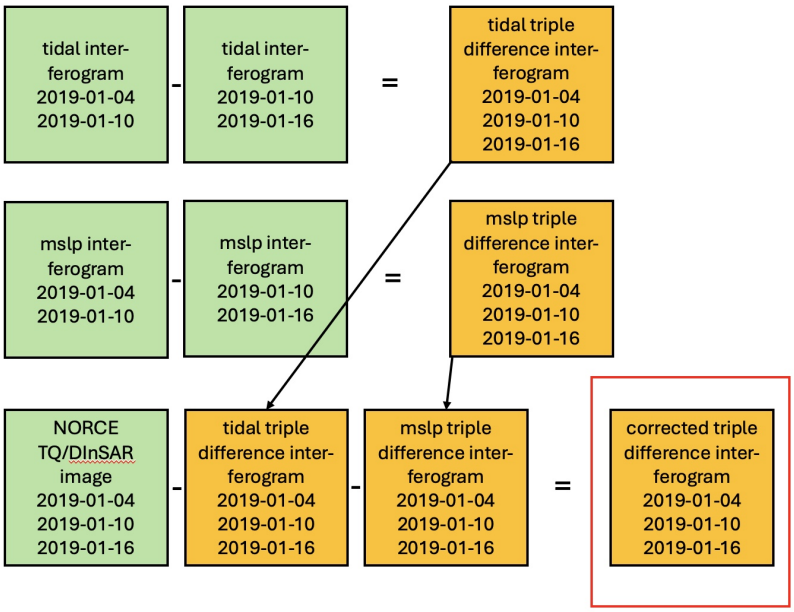

Figure 5.8: The processing chain for correcting a T/Q-DInSAR image for tides and mslp, displaying an example of a triple DInSAR image correction. The green boxes indicate input (can be from previous steps), and the yellow boxes indicate output. The red rectangle box points to the resulting image.

The same holds for generating mslp triple or quadruple difference interferograms. To correct the a T/Q-DInSAR image for tides and atmospheric pressure, the corresponding tidal T/Q difference interferogram and the corresponding mslp T/Q difference interferograms, are each are subtracted from the T/Q-DInSAR image through multiplication with the complex conjugate.

5.4 Plotting the components of the correction

Plots of the tidal- and mslp T/Q difference interferograms and their individual and combined effects on the corrected T/Q-DInSAR image are made. The plots contain the following:

- the original T/Q-DInSAR image: uncorrected, containing all displacement signals
- the T/Q-DInSAR image corrected only for mslp: containing all displacement signals except the one from mslp
- the T/Q-DInSAR image, corrected only for tides: containing all displacement signals except the one from tides
- the T/Q-DInSAR image, corrected for mslp and tides: our resulting image. According to the hypothesis, this image should not contain any remaining displacement signals
- the T/Q difference mslp interferogram: containing only the mslp displacement signal (this interferogram is masked with an ocean mask of DML for easier interpretation)
- the T/Q difference tidal interferogram: containing only the tide displacement signal
- the T/Q difference mslp+tidal interferogram: containing both the mslp and the tide displacement signals

An example of a plot with the tidal and mslp-components can be found in Figure 5.9. They are displayed in satellite geometry (range-azimuth). When analysing the tidal- and mslp components, the direction and number of fringes of these are referenced to as "ramps", since they display a height difference across the image.

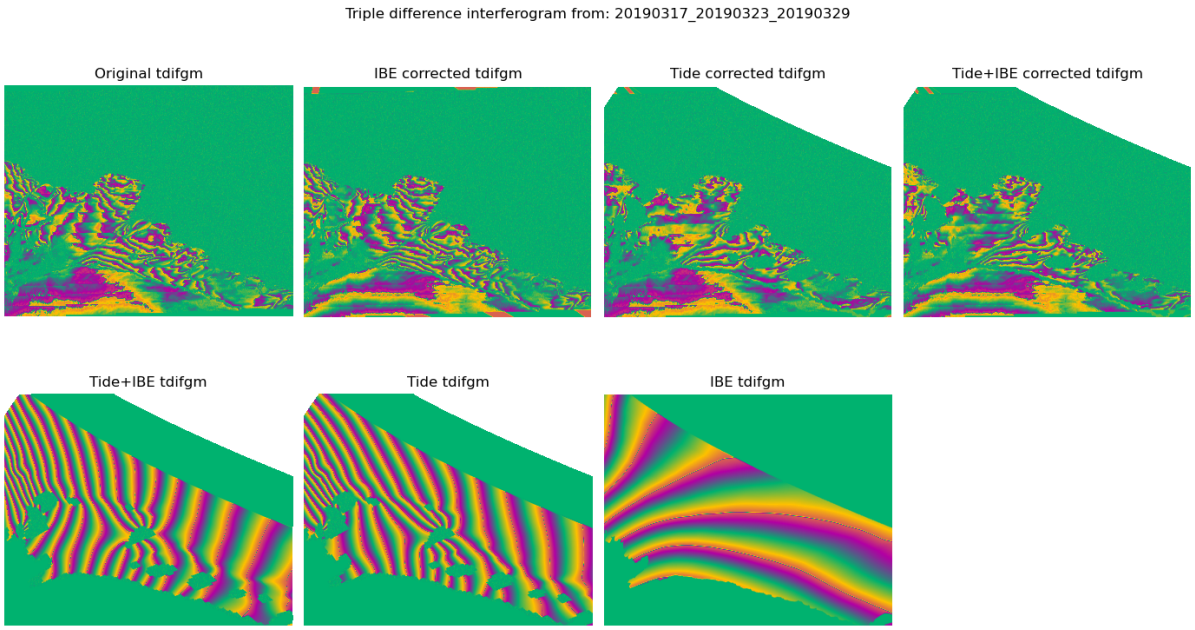

Figure 5.9: The tidal and mslp (IBE) components and their effect on the correction of the triple interferogram (tdifgm) from dates 20190215-20190221-20190227.

Chapter 6

Results and discussion

In this Chapter, the results of the tidal- and atmospheric pressure corrections on the T/Q-DInSAR images are presented, analyzed and discussed. In section 6.1, the overall remaining effects after the tidal- and atmospheric pressure correction of the T/Q-DInSAR images is shown. In section 6.2, three areas on Fimbulisen with particular characteristics after the correction are distinguished. In section 6.3, analysis of the roles of the tidal- and atmospheric pressure components in the correction is presented. Section 6.4 shows a possible link in the results to ocean eddies. Finally, section 6.5 mentions some limitations of the methods used.

6.1 Tidal- and atmospheric pressure correction

In total, 100 T/Q-DInSAR images (50 Triple combinations, 50 Quadruple combinations) were corrected for tides and atmospheric pressure. Out of these, 58 had high enough coherence to use for the data analysis. September and April data were the months most affected by coherence loss. Coherence loss can be affected by for example snowfall or snow drift. Extended periods without coherent data limits the data analysis, since it creates gaps in the T/Q-DInSAR time series. This limitation is however inherent to interferometry, since SAR-sensors are sensitive to surface back-scattering properties, linked to i.e. target water content and surface roughness.

The remaining 58 images are used for the continued analysis. An example of a T/Q-DInSAR image is shown in in Figure 6.1. Note that the T/Q-DInSAR images are shown in satellite geometry (range-azimuth) in this chapter (if not labelled otherwise). The grounded ice is masked in the resulting images; hence will show the grounded ice as a green area (value 0).

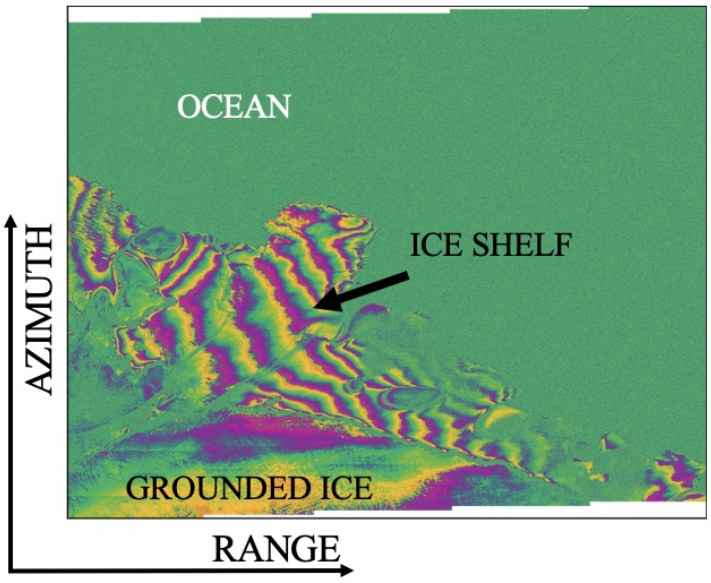

Figure 6.1: An example of T/Q-DInSAR data in satellite coordinates, with annotations pointing to the ocean (green area), ice shelf (fringed area) and grounded ice (less fringed area).

If the tidal and atmospheric pressure data can explain all the effects in the images, it is expected to have **no fringes left** in the corrected T/Q-DInSAR data. Out of the 58 coherent corrected images, there were **no images** that could be considered **completely corrected in the entire scene**. By well corrected, it is meant that the results show a "flat" interferogram with no visible coherent fringes left after correction with both tidal and mslp data.

The images show a spread of how close they were of being completely corrected. There were especially **four** images that were close to a completely corrected appearance; which displayed a few (1-4), geographically spread out fringes and therefore a visually "flat" appearance. Both their original and corrected appearances are shown in Figure 6.2. Further analysis of these four images' tidal- and mslp components is presented in section 6.3.

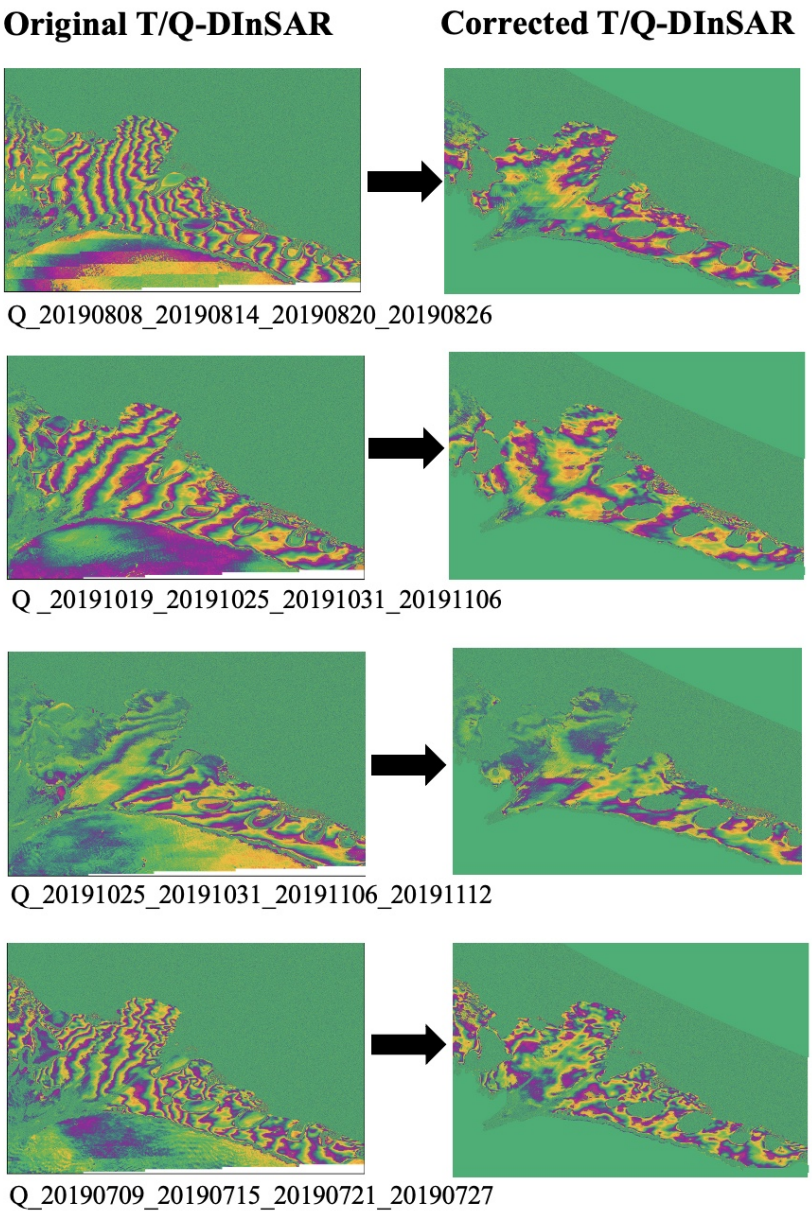

Figure 6.2: Four images close to being completely corrected. The left column shows the original T/Q-DInSAR images, and the right column shows the corresponding T/Q-DInSAR images corrected for tides and mslp.

The other **54** images of the corrected T/Q-DInSAR data had a less "flat appearance" than the ones shown in Figure 6.2. Four examples of these are found in Figure 6.3. Some of the corrections added, instead of removed, fringes to the image, which is discussed in section 6.3.

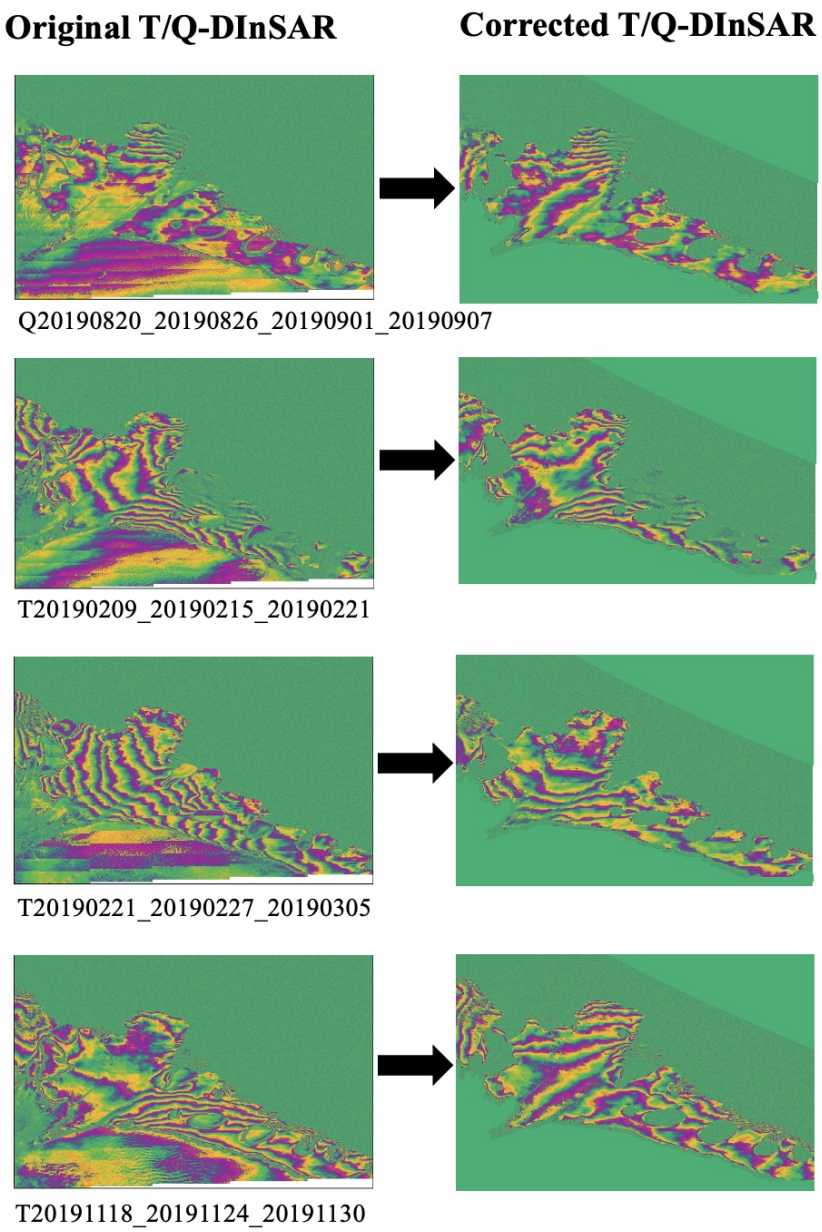

Figure 6.3: Four images far from complete correction. The left column shows the original T/Q-DInSAR images, and the right column shows the corresponding T/Q-DInSAR images corrected for tides and mslp.

A reason why no images were characterized as completely corrected, is due to the choice of threshold for this categorization. A threshold of no fringes in the entire scene is too strict; allowing no fringes (2.7cm height difference) in the entire 400km wide scene. Sun et al. (2022) showed that tide models in Antarctica disagree with each other with about 5 cm in the open ocean [22], so it can not be expected that CATS2008a have an accuracy higher than this in a complex ice shelf area. Moreover, the sufficiency of the correction relates to how close the fringes are together geographically, and how many fringes there were in the original. For better categorization of the images' correction in the future, it is suggested to instead base it on the amount of subtracted fringes from the original image, and how geographically close the remaining fringes are.

No matter the categorization, an insufficient correction can be linked to one of the following reasons:

- Inaccuracies in the tide- and atmospheric pressure models, in line with the fact that the feature rich Antarctic coastline makes accurate tidal prediction is especially challenging [22][54].
- Other significant factors affecting the vertical movement of Fimbulisen, not linked to tides or at-

mospheric pressure, e.g., cyclonic ocean eddies entering the main cavity of Fimbulisen, and affecting the surface elevation [68][101].

It is not trivial to distinguish between what remaining phase components come from errors in model output, and what comes from other geophysical factors. The continued analysis of the images however led to the identification of three different areas of Fimbulisen which often have their own particular appearance after the correction. This is shown in the next section.

6.2 Geographically distinct areas on Fimbulisen with leftover phase components

Three areas on Fimbulisen can be distinguished, each displaying particular appearances in the majority of the corrected data. These are indicated in Figure 6.4, and are:

- A. The main/central cavity of Fimbulisen
- B. The eastern part of Fimbulisen
- C. Trolltunga

These three areas are chosen as the most interesting ones in this thesis because of their to the author most intriguing appearances, and to limit the extent of the data analysis. There are other areas of Fimbulisen not analysed here; the Western part of the main cavity and the whole grounding zone area upstream of the ice shelf. These are areas that also might be interesting for analysis in the future.

When analysing the areas, a condition for being **sufficiently corrected** is established: meaning that there is **zero to one coherent fringe left in the area after correction**. All other appearances are characterized as **insufficiently corrected**.

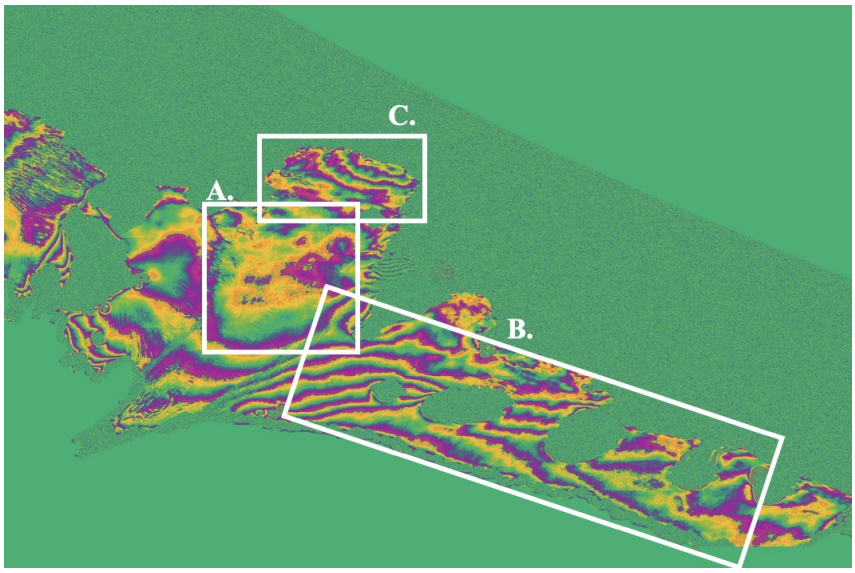

Figure 6.4: The three areas of Fimbulisen with their own particular appearance after correction: A. Trolltunga, B. The main cavity of Fimbulisen, C. The eastern part of Fimbulisen. The underlying image is the corrected T-DInSAR image from dates 20190215-20190221-20190227.

6.2.1 A. Main cavity of Fimbulisen

The main cavity of Fimbulisen (area A. in Figure 6.4) is distinguished since it is commonly the area with **least remaining phase components** out of the three areas after correction. In 38 out of the coherent 58 images, the area is sufficiently corrected. Also when the other areas are heavily fringed after correction, this area can be free from fringes. This implies that the vertical movement of the main cavity of Fimbulisen is often well resolved by the tidal- and atmospheric pressure datasets. Explanations for this could be that this area is freely floating without being locally grounded by ice rises and rumples, and

thus responds as expected to sea level fluctuations from the tidal- and atmospheric pressure forcing. See examples of the appearance in area A in Figure 6.5

In the remaining 20 images with more than 1 fringe left, the fringing is generally still more sparse than in the two other areas. This further implies that this area's vertical movement is best resolved by the two datasets. The direction of the remaining fringes does not seem to have a particular pattern, as there is a spread among fringing in the North-South direction, the East-West direction and several rotations in between these directions. This could imply that the remaining phase component here relates to small errors in the tidal and atmospheric pressure ramps, perhaps through interpolation errors (as the methodology demands interpolation of the model data to fit the satellite data) or possible output inaccuracies in the models. External oceanic forcing might show up with more consistent directions or strengths in the remaining fringe patterns.

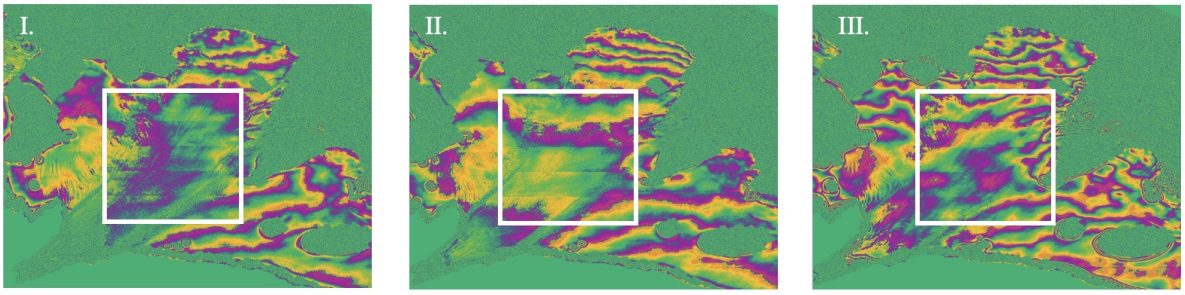

Figure 6.5: I.,II.,III: Three example images from the corrected T/Q-DInSAR data where the main cavity of Fimbulisen is sufficiently corrected, while the other areas remain insufficiently corrected.

The remaining phase components observed in area A implies that in ice shelf areas with ice in hydrostatic balance, protected from other external forcing from the Southern Ocean, it can expected of the models to adequately account for vertical movement. This is important to know when correcting for tidal and atmospheric pressure "noise" over ice shelves to retrieve smaller scale signals, when studying for example ice shelf thickness change, like in [21].

6.2.2 B. East side of Fimbulisen

The east side of Fimbulisen (area B in Figure 6.4) is distinguished as an area which is commonly **heavily fringed after correction**. Out of the 58 coherent images, 16 are sufficiently corrected, 40 are insufficiently corrected and two are discarded because the coherence was too low in this area. The insufficiently corrected images have a range of number of remaining fringes, from a few fringes spread out over the entire area, to many dense fringes over the entire area. In Figure 6.6, three examples of common appearances in the East side of Fimbulisen are shown.

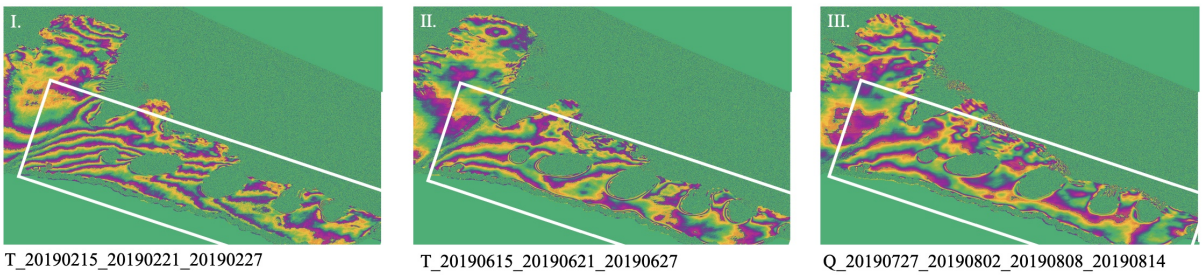

Figure 6.6: I.,II.,III: Three example images from the corrected T/Q-DInSAR data where the East side of Fimbulisen is insufficiently corrected.

The direction of the remaining fringes are commonly in the North-South direction (33 out of 40 cases)

and the rest has an East-West direction (7 out of 40 cases). This indicates that there is a pattern in the remaining fringe direction in the correction, which means that the tide- and mslp models are not sufficiently explaining the vertical movement going on in this area. A reason for this could be that **the tide model is not resolving ice flexure caused by ice rises and rumples** which grounds the ice locally. Also, within the east side of Fimbulisen, the west side is commonly more fringed after correction than the right side of this area. This might be explained by the left side being a shear zone (mentioned in Chapter 3.1.3). The shear zone divides the ice shelf in one fast flowing part (left) and one stagnant slow moving part (right). These areas are physically bound together in the ice shelf, but will possibly have different responses to oceanic forcing (one part could for example lift more than the other, leading to flexure in between them). The models are again not resolving these complex behaviors, leading to more remaining phase components in this area.

6.2.3 C. Trolltunga

Trolltunga (area C in Figure 6.4) is distinguished in the results as an area which commonly has **remaining fringes in distinct patterns after correction**. In 43 out of the 58 coherent images, Trolltunga is not sufficiently corrected for fringes, as it displays more than one fringe. There are two common appearances on Trolltunga when it is not sufficiently corrected: a **dense ramp of fringes** (36/58 cases), most commonly in the North-South direction (31/58 cases), and/or an "eye" (15/58 cases) displaying a **round fringe pattern**. Three examples of images displaying these appearances is shown in Figure 6.7.

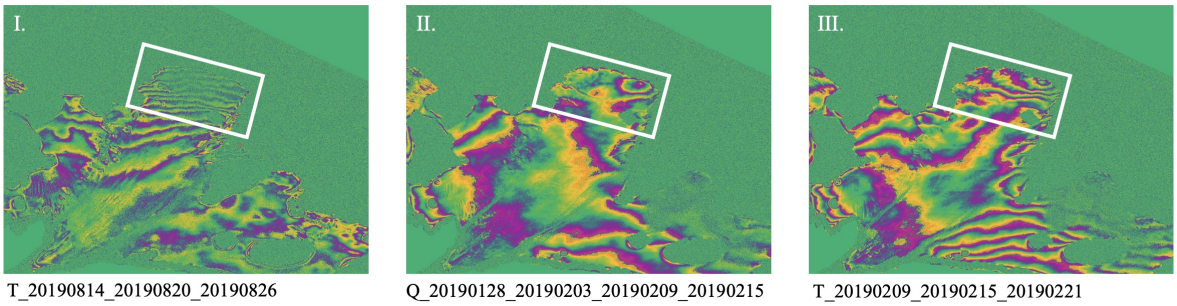

Figure 6.7: Three example images from the corrected T/Q-DInSAR data where Trolltunga is displaying common appearances: I. A densely fringed ramp in the North-South direction. II. An "eye" on the East side of Trolltunga. III. A small "eye" together with a ramp on Trolltunga.

The insufficient correction here likely has to do with effects induced from other oceanic processes in the Southern Ocean, as Trolltunga extends out into the Southern Ocean and overhanging the continental shelf break, see Figure 3.6. Trolltunga is for example subject to interaction with the Antarctic slope current and its possible pathways across this area, as indicated by [68]. The remaining fringe patterns are either dense fringe ramps or round fringe patterns, which arguably are not inherent to tidal or atmospheric pressure imprints, at least as they are known from their datasets (see later in section 6.3). In addition, Trolltunga is a more free floating area than the east side of Fimbulisen (locally grounded on the sides by small ice rises or rumples), so it could be argued that it is not subject to the same amount of flexure due to tides.

When further investigating North-South ramps on Trolltunga, the color-cycle is in different directions from image to image. In several T/Q-combinations following one another in a time series, the ramp apparent at Trolltunga can be seen **changing to the opposite direction in each acquisition following the last**. See an example of this in Figure 6.8.

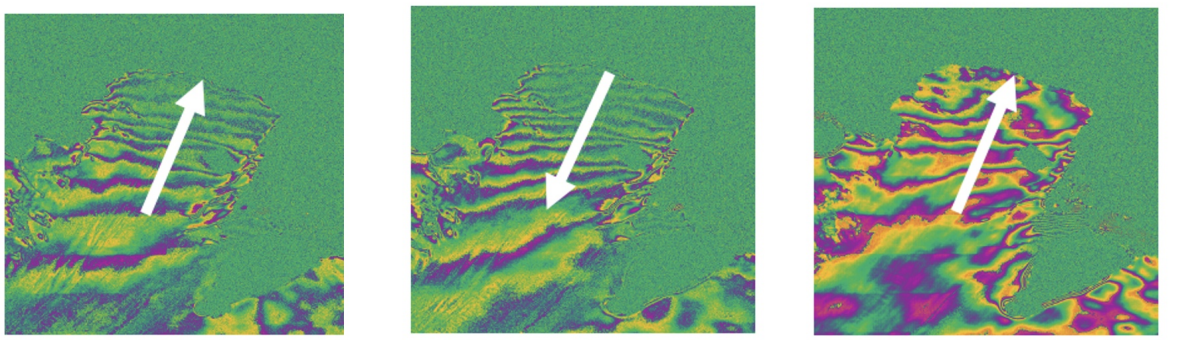

Figure 6.8: Three T-DInSAR combinations following one another, where the ramp at Trolltunga changes direction in each image. The arrows indicate the direction of relative uplift (color-cycle green-purple-yellow). I. A ramp with a Northward relative uplift. II. A ramp with a Southward relative uplift. III. A ramp with a Northward relative uplift.

These ramps are likely associated with Trolltunga flexing up or down in any/several of the acquisitions. The reasons for the ramps to change direction in the combination following the last, is however not trivial to distinguish, because of how the triple and quadruple differences are structured. The change of direction could be due to the tongue being in a higher position in one of the acquisitions in one combination, and then this high position acquisition is used in the next combination too, but shifted to a term of the opposite sign in the difference, turning the direction around. Or, the tongue could be moving up and down between each acquisition in the differences, causing the direction to shift. This points to that double difference interferograms are not trivial to interpret, as there are three or four components in a specific order which make up the final image.

The ramps can also link to oceanic processes in the Southern Ocean. Trolltunga is exposed to the Antarctic Slope Current, which moves westward along and underneath it where it overhangs the continental shelf break [68]. The presence of a current underneath Trolltunga could affect the height of it, since ocean currents affect the sea surface height (SSH) [102], however it is not known by how much, and if it would be significant enough. However, it is known that the strength of Antarctic Slope Current vary seasonally [103], so future work could include analysing the timing of the ramps appearing at Trolltunga and connect them to the current strength seasonality.

Another factor that has the potential to alter the vertical movement of Trolltunga, is wind driven surface elevation. This is mentioned in Chapter 3.2.2 as a factor that can be significant enough to compare with tidal effects [76]. If the wind strength is significant and the direction is towards Trolltunga, the wind could push water in under the ice tongue, raising it. To further investigate if wind driven elevation effects could be present, it would be relevant to look into wind strength, wind direction and significant wave height data from the ocean around Fimbulisen. It would possibly be less likely to cause elevation in the austral winter months, because of the presence of sea ice and less such wind driven effects. The ramps on Trolltunga do however exist in the data all year round, which indicates that it could be multiple oceanic processes causing imprints in the data.

The results from the areas in this section, indicate that the characteristics of the different regions within an ice shelf should be carefully considered when correcting data acquired over ice shelves for tides and atmospheric pressure. The more it is known about ice shelf structures and their individual response to tides, atmospheric pressure and other factors affecting their vertical movement, the more the correction can be optimized. With such knowledge, it is also possible to quantify the error margins and uncertainties in tidal- and atmospheric pressure corrections in ice shelf areas. For example, an assessment and improvement of 'traditional tidal modelling' output was made in a doctoral thesis by C. Wild (2018) over an Antarctic ice shelf using T/Q-DInSAR and in situ data [54], see Chapter 3.3. Through more extensive processing techniques on the T/Q-DInSAR data like [54], it can be possible to find the uncertainty of tide model output, and also improve the prediction of the tidal movement of an ice shelf. For further work with large swath T/Q-DInSAR data over Fimbulisen, similar processing techniques could be applied the data, to find the quality of, and improve, the tide model output.

6.3 Role of the tidal- and atmospheric pressure components in the correction

The tidal- and mslp components and their possible effects on the correction are analyzed for the 58 coherent images in the dataset (triple and quadruple combinations) through plots displayed in Figure 5.9.

6.3.1 Tidal component

The tidal component of the correction is the **largest component**. In the tidal T/Q-DInSAR combinations, there tidal T/Q-difference interferograms show 6 to 40+ fringes, in different directions. The direction of these fringes is mostly homogeneous throughout the scene, creating a "striped" scene see Figure 6.9. The striped scene indicates that the tidal height differences are similar in one direction across the scene. The most common direction of the fringes is in the East-West direction with 30/58 cases, the North-South direction has 17/58 cases and 11/58 cases have any 45 degree angle direction between these directions, see Table 6.1.

Table 6.1: The distribution of the tidal ramp direction among the 58 coherent images

Direction of tidal ramp	**East-West**	**North-South**	**45 degrees**
Amount (percentage) of all tidal interferograms	30/58 (53%)	17/58 (29%)	17/58 (19%)

All investigated triple combinations except one (with 16 fringes) contain over 20 fringes, while only 7 (out of 30) of the quadruple combinations contain over 20 fringes. As mentioned in Chapter 2.4, a triple combination takes the middle phase image into account twice, and can therefore enhance its contribution, which explains the triple differenced tidal images having more dense fringe patterns.

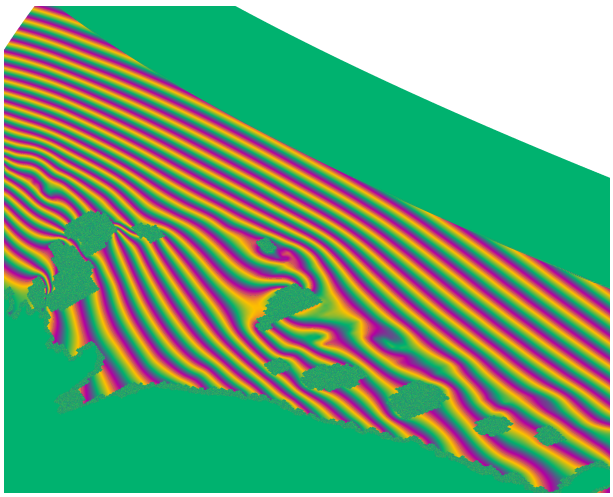

Figure 6.9: A triple difference tidal interferogram in satellite geometry of track 60 from dates 20190814-20190820-20190826. The tidal pattern is striped in the North-South-direction.

The tidal component removes fringes from the original T/Q-DInSAR images in all 58 cases but two, where it adds instead of removes fringes throughout the entire scene. In these two cases, the tidal ramps are quite low (quadruple combinations with 10 and 12 fringes in the tidal image). These are possibly tied to a tide model output where the sign of the output tidal heights is the opposite to the real tide. This could likely occur at around zero tide, where even a small miscalculation of tidal output could change the sign of it. This could result in the tidal double difference interferogram having phase components in the opposite direction than the real tidally induced effects in the T/Q-DInSAR imagery, hence adding instead of removing fringes in the scene.

Correlation between the tidal component and the correction

Since the tidal component is the largest component of the correction, it is investigated if there is a correlation between a better correction and the tidal ramp's direction and strength. This is done for the four images close to being completely corrected T/Q-DInSAR images shown in Figure 6.2:

- 20190709-20190715-20190721-20190727: 20 fringes, East-West direction
- 20190802-20190808-20190814-20190820: 30 fringes, East-West direction
- 20191019-20191025-20191031-20191106: 15 fringes, East-West direction
- 20191025-20191031-20191106-20191112: 6 fringes, North-South direction

In the cases closest to complete correction, a wide range of tidal ramp strengths are represented. Due to this, and the few cases investigated, no conclusion can be drawn on if the tidal ramp's direction and strength have affect on the sufficiency of the correction. If more data from other years would be analysed, perhaps a possible link between tidal ramp and sufficient corrections could be found. However, if no link is found, it could indicate that the remaining phase components might not have to do with the tide model output accuracy, but the atmospheric pressure model output accuracy or other geophysical factors affecting Fimbulisen's vertical movement.

Each of the three areas are investigated for the sufficient/insufficient correction's connection to the tidal ramps. The direction of the tidal ramps are investigated for the deviating 'correction trend' (that is, the correction, insufficient or sufficient, that is the minority in each area), meaning:

- the 20 insufficiently corrected cases of area A
- the 15 sufficiently corrected cases of area B
- the 15 sufficiently corrected cases of area C

This is done to see if the tidal ramps of these images have a similar distribution of tidal directions and sizes as the entire set of tidal dd-interferograms. See Table 6.2 for this distribution of each area, with the distribution of the entire set of tidal double difference interferograms (dd-interferograms) at the bottom.

Table 6.2: The tidal ramp directions, and range of number of fringes for T: Triple combinations and Q: Quadruple combinations, for the tidal ramps connected to the images with the 'deviating correction trend' of each area.

	East-West	**North-South**	**45 degrees**	**No. of fringes (range)**
Area A	12/20 (**60%**)	5/20 (**25%**)	3/20 (**15%**)	T: 16-30 Q: 7-30
Area B	10/15 (**67%**)	3/15 (**20%**)	2/15 (**13%**)	T: 15-30 Q: 6-30
Area C	8/15 (**53%**)	4/15 (**27%**)	3/15 (**20%**)	T: 20-40 Q: 6-20
All tidal dd-interferograms	30/58 (**53%**)	17/58 (**29%**)	17/58 (**19%**)	T: 11-40+ Q: 6-30

In Table 6.2, the distribution of the tidal directions is very similar to the total tidal interferogram distribution in area C. There is a slight bias in area B towards the East-West correction, possibly implying that this direction of the tidal ramp would worsen the correction of the Eastern part of Fimbulisen. An even smaller such bias is found for area A. More data might be needed to see if this bias is significant enough to draw any conclusions about the tidal ramp's direction's effect on the resulting correction.

However, area C seems to be least affected by the tidal ramp's direction for an insufficient correction - possibly implying that this area's appearance after tidal correction might not have to do with tides, but perhaps other factors, mentioned in section 6.2.3 and 6.4.

For the tidal ramp's strength, represented by "No. of fringes (range)" in Table 6.2, there is a distribution across almost all tidal ramp strengths in area A and B, and a slightly higher number of fringes in area C. However, the range of fringes is still large in each area and any links to low/high tidal ramps are not clear to find.

From the data analysis made in this thesis, it is not clear if the tidal model performs better or worse at certain tidal stages. The tidal component adds fringes to the whole scene in 2/58 cases, which indicates that the tidal model has the potential to worsen the correction, possibly tied to low tidal stages. However, it is seen that the tidal model removes phase components in the rest of the data, and is especially good at resolving the free floating main cavity of Fimbulisen, as high tidal ramps can be completely removed in the correction of this area. The tidal model component is also performing better than the atmospheric pressure model component (when looking at the number of cases it worsens the correction). This is expected, as the former is a regional model and the latter a global model.

By using CATS2008a, it is possible to remove many fringes from large ramps in the T/Q-DInSAR data (up to 40 fringes). This has enabled us to identify imprints from possible other geophysical factors throughout the dataset. Hence, CATS2008a can be used to remove a significant amount of the "tidal noise" in T/Q-DInSAR data over ice shelves, and can create possibilities to tie some of the remaining signals to geophysical processes of the ice shelf.

6.3.2 Atmospheric pressure component

The atmospheric pressure component is **smaller than the tidal component**; from 0 to 10 fringes over the scene. The fringing is less homogeneous over the scene compared to the tides, as it displays ramps which commonly change direction and fringe density across the scene, see an example in Figure 6.10. This less homogeneous pattern can be explained by the nature of atmospheric pressure versus tides: the tides are highly periodic in nature, in when and from which direction they move. Atmospheric pressure is connected by "less periodic" weather fronts, which come at inconsistent times, from different directions and with different speeds, and might deviate more in strength and direction across the scene.

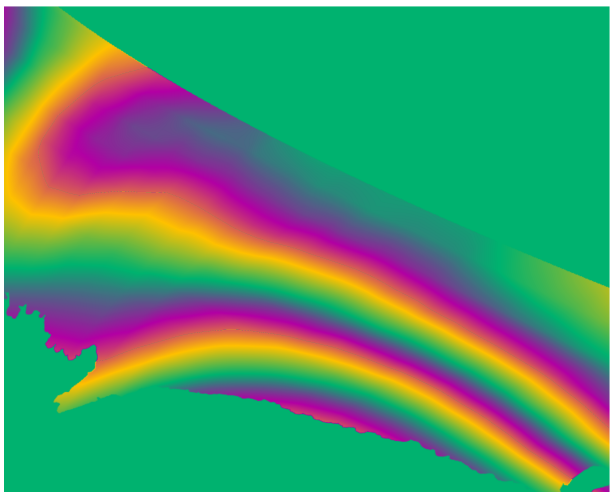

Figure 6.10: A masked triple difference mslp interferogram in satellite geometry of track 60 from dates 20190703-20190709-20190715.

Correlation between the atmospheric pressure component and the correction

The mslp-component's size is investigated for the cases closest to complete correction, and for cases where this component worsens the correction across the scene. For the mslp-component, it is not possible to associate each correction with one direction of the ramp, since it often changes its direction across the scene.

For the four cases closest to complete correction, the mslp component's number of fringes is:

- 20190709-20190715-20190721-20190727: 0 fringes
- 20190802-20190808-20190814-20190820: 4 fringes
- 20191019-20191025-20191031-20191106: 1 fringes
- 20191025-20191031-20191106-20191112: 3 fringes

This could possibly indicate that a small atmospheric pressure component from ERA5 can be a prerequisite of a well corrected image. However, more close to well corrected images in datasets from longer time series need to be analysed to strengthen this.

The mslp correction removes fringes from the entire scene in all 58 cases but 11; where it worsens the overall correction (in all areas). These 11 cases have 2-8 fringes in their mslp-component, which means it is unclear if a certain strength of the mslp ramp ties to a worsening of the correction.

Since a possible link between a small atmospheric pressure component and improved correction in images was observed, and the fact that it worsens the correction in 11/58 cases, it indicates that the atmospheric pressure model is worse at correcting the images than the tidal component. This difference is expected, as the global atmospheric pressure data has lower spatial resolution compared to the regional tide model, and can therefore not resolve regional areas equally well. Moreover, a more extensive interpolation is needed to fit this dataset to the resolution of the T/Q-DInSAR data. A possible implication from this could be that one should be careful when choosing the atmospheric pressure dataset around the Antarctic coastlines. A more ideal dataset could be provided by for example multiple in-situ weather stations, continuously measuring atmospheric pressure, combined with GPS height stations on ice shelves, which was used in previous work by C. Wild [54]. However, this work was conducted over a much smaller ice shelf, and might not be easily transferable to correcting S1 EW imagery over Fimbulisen, as the study area is much larger.

The T/Q-DInSAR data is composed of several snapshots in time at different tidal heights and atmospheric pressure anomalies, making it challenging to disentangle the influence that each component has on the resulting image. Even though an effort to relate the result to some of its components was made in this thesis, it is clear that more investigations would be beneficial, among the tidal- and mslp double difference interferograms, the tidal- and mslp single interferograms and the tidal- and mslp single snapshots. Such an analysis would be time consuming and depend on a lot of parameters. Another way forward could be to use other regional tide models of Antarctica on the same images with the same combination of ERA5, to decide which regional tide model is working most sufficiently over Fimbulisen.

Finally, a limitation on the accuracy for the tidal- and atmospheric pressure data is that it is interpolated in time. The tide model output is subject to interpolation from 4km, to 1km, to InSAR geometry $\approx$100m, and this will lower the accuracy of the output across the scene. The accuracy of the ERA5 output will likely be even lower, since the interpolation is more extensive (about 30km to InSAR geometry $\approx$100m). In future similar work, a more high resolution atmospheric pressure model could be desired, i.e. the MAR model designed for polar regions [104].

6.4 Possible ocean eddy imprint in the images

In the analysis of the images, a hypothesis is that the round fringe patterns, or "eyes", at Trolltunga could possibly be **linked to cyclonic ocean eddies underneath the ice shelf**. Cyclonic ocean eddies under Fimbulisen have been linked to coincide with warm deep water intrusion [68]. Warm deep water intrusion is associated to higher temperatures in the M1 mooring data (see Chapter 4.4 and Chapter 3.1.3), and the temperature from M1 lower from 2019 are plotted in Figure 6.11. The plot is overlaid with marks of the dates from T/Q-DInSAR combinations which display an eye at Trolltunga. The temperature data used has one daily average output each day, so only the dates from the S1 overpasses, and not the full timestamps, are associated with the temperature in the mooring data.

The dates with high temperatures chosen to be investigated, are involved in the following T/Q-DInSAR images displaying round fringe patterns:

- Triple combination 20190128-20190203-20190209
- Quadruple combination 20190128-2019020203-20190209-20190215
- Triple combination 20190203-20190209-20190215
- Triple combination 20190209-20190215-20190221
- Quadruple combination 20190323-20190329-20190404-20190410
- Triple combination 20191007-20191013-20191019

Unfortunately, the T/Q-DInSAR combinations generated from the highest peaks in the plot in Figure 6.11, in September, suffered from loss of coherence.

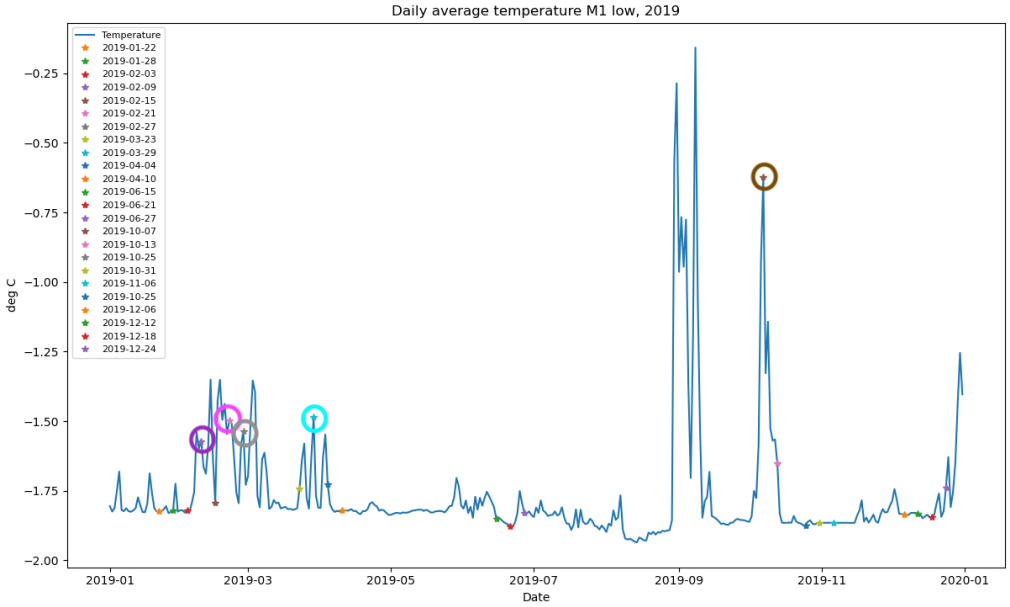

Figure 6.11: The temperature data from M1, together with the dates of the relevant available T/Q-DInSAR data. The circled points indicate the high temperature days, which also was included in an available T/Q-DInSAR image with a round fringe pattern, which were chosen to be investigated. These dates are: 2019-02-09 (purple), 2019-02-15 (pink), 2019-02-27(gray), 2019-03-29 (blue) and 2019-10-07 (brown).

The geocoded versions of these T/Q-DInSAR combinations over Trolltunga, can be found in Figure 6.12. The diameter of one round fringe pattern in each image are manually measured in QGIS in randomly chosen direction across the round pattern. From this the size can be estimated, and the number of outside-to-center fringes of the imprints are also observed. The measurement lines on the patterns are displayed in Figure 6.13. Their diameters are in the range of 10-25 km, though they vary somewhat in size and shape, and also in the number of fringes.

Combinations Q20190128-2019020203-20190209-20190215 and T20190209-20190215-20190221 display more than one, but less than two color cycles (i.e. purple-yellow-green-purple) from the outer part of the pattern to the centre of the pattern. The rest of the combinations show less than one fringe cycle. This means that the outside to centre surface change of these observed patterns is about 5 cm or less. The measured length of the lines in Figure 6.13, and each pattern's outside to centre (inward) color cycle are shown in Table 6.3.

Combination	Distance (km)
T20190128-20190203-20190209	17.0
Q20190128-2019020203-20190209-20190215	23.4
T20190203-20190209-20190215	11.5
T20190209-20190215-20190221	15.4
Q20190323-20190329-20190404-20190410	17.3
T20191007-20191013-20191019	13.3

Table 6.3: A distance across the investigated circular imprints in the T/Q-DInSAR combinations

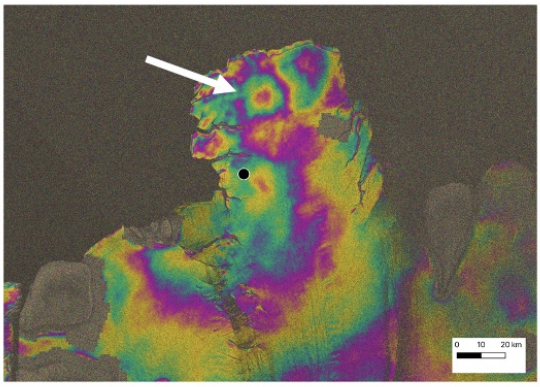

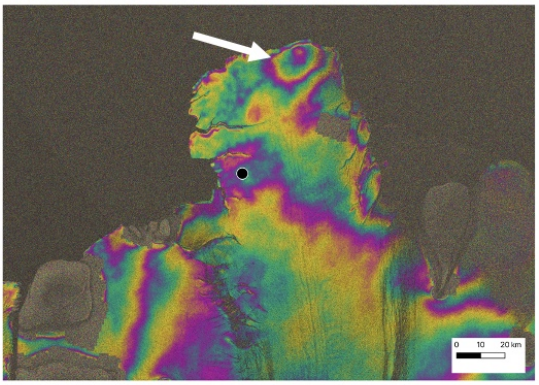

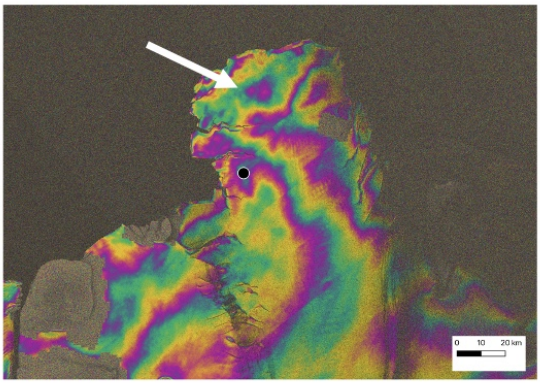

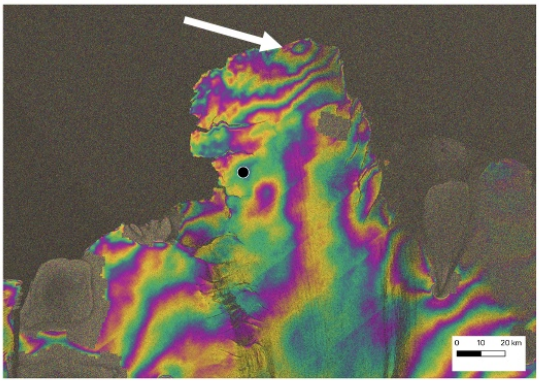

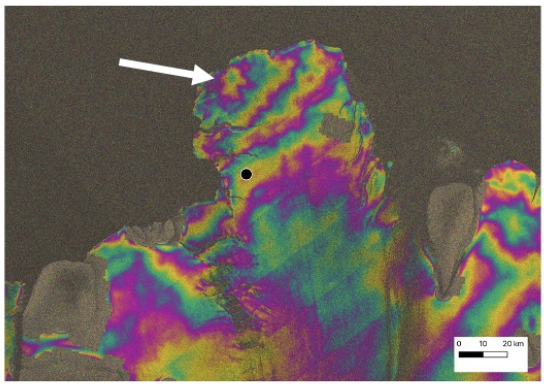

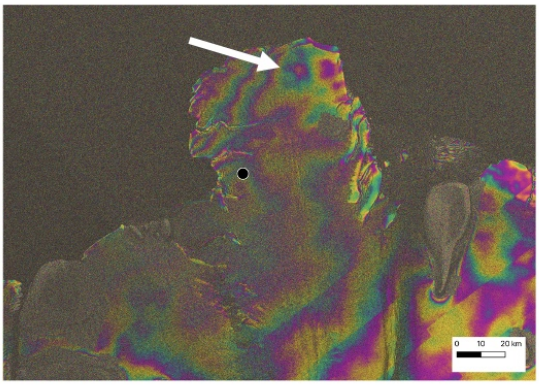

Figure 6.12: The geocoded versions of the combinations containing round fringe-patterns, over Trolltunga (on EPSG:3031). The white arrow points to some of the round fringe patterns. The black dot in the images indicates the location of mooring site M1. The interferogram coherence is overlaid the interferograms, and darkens the image where coherence is lower.

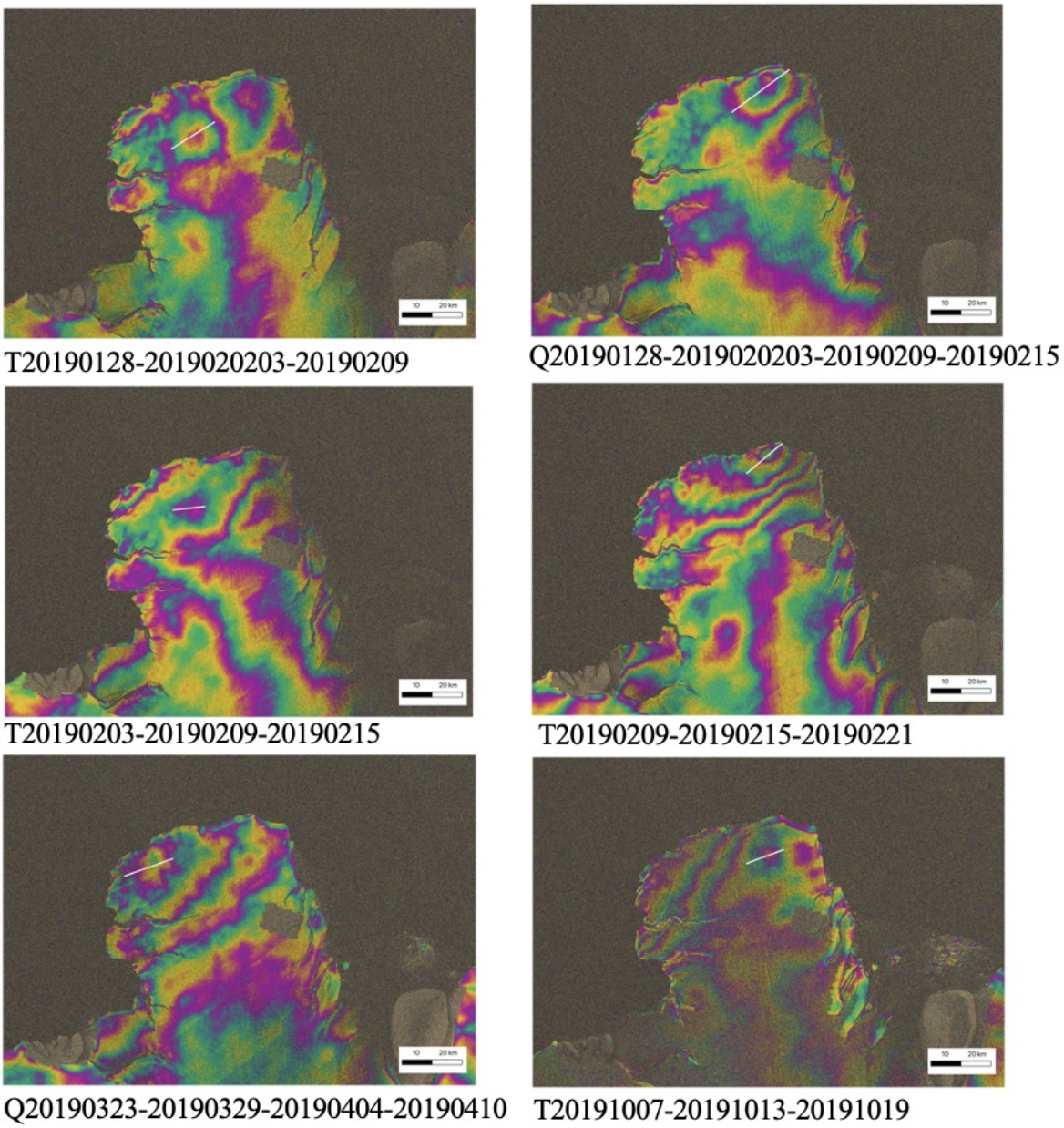

Figure 6.13: The lines measured to represent a diameter of the round fringe pattern, on the combinations containing round fringe-patterns over Trolltunga (on EPSG:3031). The lengths of these lines are presented below.

Relating the circular imprints to a surface expression, i.e. outside to center uplift or subsidence, is non-trivial since the T/Q-DInSAR imagery stem from three or four acquisitions, and are relative differences. The color cycle seen in the images are therefor not directly relatable to ocean surface uplift or subsidence by simply looking at them. The surface expression has to be disentangled to the acquisition date it stems from and its position in the T/Q-DInSAR equations 2.8 or 2.9. This could possibly be done with assumptions of each circular surface expression stemming from only one date with high temperatures in Figure 6.11, in its T/Q-DInSAR combination. If such a method would generate similar surface expressions, these could possibly be linked to theory about eddy surface expressions, as it is known that eddies can create uplift or subsidence of the ocean surface [101].

Also, more than one round fringe pattern can be observed in Figure 6.12, and this could be due to one out of two things. 1) if there is only one of the single images in the combination containing eddies, there could be a chain of multiple eddies under the ice shelf. Alternatively, 2) if more than one of the single images in the combination containing eddies, it could be the same eddy observed in two succes-

sive SAR acquisitions, possibly shifted across the ice shelf. This hypothesis would have to be aligned with theory of how eddies move and the length of their lifetime.

To sum up the characteristics of the round fringe patterns, they have diameters of 10-25 km and are characterized by a surface expression (of unknown direction) of less than 5 cm from the outside to the centre. In [68] the mean radius of a cyclonic ocean eddy connected to high mooring temperatures was estimated to 8 km, something that can align with the measured diameters of the round fringe patterns. Further, the round fringe patterns were in all cases but one detected in imagery from months that typically see more eddies [68]. These findings support the hypothesis of the circular imprint being associated with the eddies observed in [68].

However, more investigations are needed to strengthen this hypothesis. Investigations using T/Q-DInSAR combinations with SAR imagery from the time of year associated with high mooring temperatures could identify if the circular imprint are statistically more likely to occur then. If more combinations are made, over extended epochs where the 'eddy'-date is differenced against dates in the months where these types of eddies typically are not present, perhaps clearer imprints could be found. Confirming these type of cyclonic eddies in the T/Q-DInSAR imagery, could lead to the possibility of monitor warm deep water intrusion, connected to basal melt of Fimbulisen, from space.

6.5 Limitations of the methods

No atmospheric corrections, in the form of for example removing ionospheric distortions, are made in the T/Q-DInSAR data, hence the images may contain remaining phase noise due to atmospheric conditions.

Another limitation of using T/Q-DInSAR over ice shelves, stems from the assumption of constant horizontal ice flow throughout the epochs. This is an idealization of ice shelf flow and might not be true in practice, so the contribution of horizontal LOS displacement might not be fully removed from the T/Q-DInSAR dataset. This could be especially true in the area of the fast flowing Jutulstraumen, where ice flow is more dynamic than in the eastern part of Fimbulisen, where it is more stagnant. This is not noted in the data analysis, and the variability of the Jutulstraumen speed within a 6 day interval could be investigated further to estimate an error margin.

Chapter 7

Conclusions and future work

The hypothesis of this thesis was that the tidal model CATS2008a and atmospheric pressure model ERA5 can explain all the displacement signals in the T/Q-DInSAR data over Fimbulisen. The first conclusion of this thesis is that the datasets could not completely do so. However, further investigation of ice shelf behavior, tide model output, and additional processes through these datasets, lead to the further conclusions and future work recommendations in this chapter.

Even though the CATS2008a and ERA5 datasets could not fully explain all displacement signals in the T/Q-DInSAR data over Fimbulisen, the combination of data did remove most of the tidal- and atmospheric "noise" in the T/Q-DInSAR imagery. To analyse the remaining phase components, the ice shelf was divided into three distinctly different areas: the main cavity, the eastern side and Trolltunga.

Fimbulisen's main cavity is well resolved by the tidal- and atmospheric pressure data, while its east side is probably subject to ice flexure that is not resolved by either tidal- or pressure corrections, due to local grounding of the ice and the presence of a large shear zone. Trolltunga displays two displacement signals, potentially connected to processes in the Southern Ocean: 1) vertical ramps, that could tie to other oceanic effects, i.e. from the Antarctic Slope Current or more likely, wind-driven surface elevation, and 2) circular imprints. These imprints were investigated for their connection to warm deep water carrying ocean eddies, through high temperatures in a mooring dataset under Fimbulisen. The circular imprints in the T/Q-DInSAR data could be linked to the size and seasonal occurrence of the eddies in [68]. The connection needs further investigation, for example by creating different T/Q-DInSAR combinations from the dates tied to high temperatures and circular imprints. Moreover, extending the time series of T/Q-DInSAR data to additional years could uncover further circular imprints in the data to be investigated. Also, linking what is observed to more theory on these types of eddies, like their exact surface expression, is needed.

The non-trivial interpretation of T/Q-DInSAR imagery made it difficult to conclusively tie remaining phase components to the exact reason they appeared, i.e. identifying fringes tied to tide model output errors. Exact knowledge about tide model accuracy was therefore not retrieved. However, it can be concluded that CATS2008a corrects for tides in well known ice shelf cavities with freely floating ice, like the main cavity of Fimbulisen. It has decreased performance over more complex ice shelf geometries, even if the bathymetry is relatively well known, as it is for Fimbulisen. ERA5 is performing worse than the tidal model, but can remove some atmospheric effects in most cases, however a high resolution regional model would be of preferred use for future work.

Finally, the combination of these two datasets can remove a significant amount of the main effects prevalent in the T/Q-DInSAR data, which made it possible to reveal other interferometric patterns, connected to bending of Trolltunga and possibly to warm water eddies under Fimbulisen. Such reveals could help us learn more about ice shelf behavior and what processes it might be subject to, which is important for expanding the knowledge about Antarctica as a key component in the climate system.

Future work includes:

- Combining T/Q-DInSAR data with other regional tidal models, and a higher resolution atmospheric pressure model, possibly along with in situ GPS height measurements like in [54], to get further to identify tide model flaws

- Use wind- and significant wave height data from the ocean outside of Trolltunga, to possibly connect the ramps seen with wind-driven surface elevation
- Investigate more combinations of the current and extended time series of T/Q-DInSAR data over Fimbulisen, to solidify a link between the circular imprints in the data and the observed ocean eddies in [68]

Chapter 8

Appendix

8.1 S1-A/B timestamps

2019-01-04 20:25:13
2019-01-10 20:24:31
2019-01-16 20:25:12
2019-01-22 20:24:30
2019-01-28 20:25:12
2019-02-03 20:24:30
2019-02-09 20:25:11
2019-02-15 20:24:30
2019-02-21 20:25:11
2019-02-27 20:24:30
2019-03-05 20:25:11
2019-03-11 20:24:29
2019-03-17 20:25:11
2019-03-23 20:24:29
2019-03-29 20:25:12
2019-04-04 20:24:30
2019-04-10 20:25:12
2019-04-16 20:24:30
2019-04-22 20:25:12
2019-04-28 20:24:31
2019-05-04 20:25:13
2019-05-10 20:24:31
2019-06-15 20:24:33
2019-06-21 20:25:15
2019-06-27 20:24:34
2019-07-03 20:25:16
2019-07-09 20:24:35

2019-07-15 20:25:17
2019-07-21 20:24:35
2019-07-27 20:25:18
2019-08-02 20:24:36
2019-08-08 20:25:18
2019-08-14 20:24:37
2019-08-20 20:25:19
2019-08-26 20:24:38
2019-09-01 20:25:20
2019-09-07 20:24:38
2019-09-13 20:25:20
2019-09-19 20:24:39
2019-09-25 20:25:21
2019-10-01 20:24:39
2019-10-07 20:25:21
2019-10-13 20:24:39
2019-10-19 20:25:21
2019-10-25 20:24:33
2019-10-31 20:25:15
2019-11-06 20:24:33
2019-11-06 20:24:39
2019-11-12 20:25:21
2019-11-18 20:24:39
2019-11-24 20:25:21
2019-11-30 20:24:38
2019-12-06 20:25:20
2019-12-12 20:24:38
2019-12-18 20:25:20
2019-12-24 20:24:38
2019-12-30 20:25:19
2020-01-05 20:24:37

Bibliography

[1] S. L. Howard, S. Erofeeva, and L. Padman. *CATS2008: Circum-Antarctic Tidal Simulation version 2008*. https://doi.org/10.15784/601235. 2019.

[2] L. Padman, H. Fricker, R. Coleman, S. Howard, and L. Erofeeva. "A new tide model for the Antarctic ice shelves and seas". In: *Annals of Glaciology* 34 (2002), pp. 247–254.

[3] T. C. Sutterley, K. Alley, K. Brunt, S. Howard, L. Padman, and M. Siegfried. *pyTMD: Python-based tidal prediction software*. https://doi.org/10.5281/zenodo.5555395. 2017.

[4] H. Hersbach, B. Bell, P. Berrisford, G. Biavati, A. Horányi, J. Muñoz Sabater, J. Nicolas, C. Peubey, R. Radu, I. Rozum, D. Schepers, A. Simmons, C. Soci, D. Dee, and J-N. Thépaut. *ERA5 hourly data on pressure levels from 1940 to present*. https://doi.org/10.24381/cds.bd0915c6. Accessed on 28-APR-2024. 2023.

[5] Copernicus Climate Change Service. *ERA5 hourly data on single levels from 1940 to present*. Accessed on 28-APR-2024. 2024.

[6] S. Dangendorf, C. Hay, F.M. Calafat, and et al. "Persistent acceleration in global sea-level rise since the 1960s". In: *Nature Climate Change* 9 (2019), pp. 705–710.

[7] S.A. Kulp and B.H. Strauss. "New elevation data triple estimates of global vulnerability to sea-level rise and coastal flooding". In: *Nature Communications* 10 (2019), p. 4844.

[8] "Sea Level Rise and Implications for Low-Lying Islands, Coasts and Communities. In: IPCC Special Report on the Ocean and Cryosphere in a Changing Climate". In: *Cambridge University Press, Cambridge, UK and New York, NY, USA* (2019), pp. 321–445.

[9] P. Fretwell, H. D. Pritchard, D. G. Vaughan, J. L. Bamber, N. E. Barrand, R. Bell, C. Bianchi, R. G. Bingham, D. D. Blankenship, G. Casassa, G. Catania, D. Callens, H. Conway, A. J. Cook, H. F. J. Corr, D. Damaske, V. Damm, F. Ferraccioli, R. Forsberg, S. Fujita, Y. Gim, P. Gogineni, J. A. Griggs, R. C. A. Hindmarsh, P. Holmlund, J. W. Holt, R. W. Jacobel, A. Jenkins, W. Jokat, T. Jordan, E. C. King, J. Kohler, W. Krabill, M. Riger-Kusk, K. A. Langley, G. Leitchenkov, C. Leuschen, B. P. Luyendyk, K. Matsuoka, J. Mouginot, F. O. Nitsche, Y. Nogi, O. A. Nost, S. V. Popov, E. Rignot, D. M. Rippin, A. Rivera, J. Roberts, N. Ross, M. J. Siegert, A. M. Smith, D. Steinhage, M. Studinger, B. Sun, B. K. Tinto, B. C. Welch, D. Wilson, D. A. Young, C. Xiangbin, and A. Zirizzotti. "Bedmap2: improved ice bed, surface and thickness datasets for Antarctica". In: *The Cryosphere* 7.1 (2013), pp. 375–393.

[10] E. Rignot, I. Velicogna, M. R. van den Broeke, A. Monaghan, and J. T. M. Lenaerts. "Acceleration of the contribution of the Greenland and Antarctic ice sheets to sea level rise". In: *Geophysical Research Letters* 38.5 (2011). eprint: https://agupubs.onlinelibrary.wiley.com/doi/pdf/10.1029/2011GL046583.

[11] R.M. DeConto, D. Pollard, R.B. Alley, and et al. "The Paris Climate Agreement and future sea-level rise from Antarctica". In: *Nature* 593 (2021), pp. 83–89.

[12] T.L. Edwards, S. Nowicki, B. Marzeion, and et al. "Projected land ice contributions to twenty-first-century sea level rise". In: *Nature* 593 (2021), pp. 74–82.

[13] The IMBIE team. "Mass balance of the Antarctic Ice Sheet from 1992 to 2017." In: *Nature 558* (2018).

[14] Eric Rignot, Jérémie Mouginot, Bernd Scheuchl, Michiel van den Broeke, Melchior J. van Wessem, and Mathieu Morlighem. "Four decades of Antarctic Ice Sheet mass balance from 1979–2017". In: *Proceedings of the National Academy of Sciences* 116.4 (2019), pp. 1095–1103. eprint: https://www.pnas.org/doi/pdf/10.1073/pnas.1812883116.

[15] J. Garbe, T. Albrecht, A. Levermann, and et al. "The hysteresis of the Antarctic Ice Sheet". In: *Nature* 585 (2020), pp. 538–544.

[16] J. Fürst, G. Durand, F. Gillet-Chaulet, L. Tavard, M. Rankl, M. Braun, and O. Gagliardini. "The safety band of Antarctic ice shelves". In: *Nature Climate Change* 6 (2016), pp. 479–482.

[17] E. Rignot, S. Jacobs, J. Mouginot, and B. Scheuchl. “Ice-Shelf Melting Around Antarctica”. In: *Science* 341.6143 (2013), pp. 266–270. eprint: https://www.science.org/doi/pdf/10.1126/science.1235798.
[18] Hamish Pritchard, Stefan Ligtenberg, Helen Fricker, David Vaughan, Michiel Van den Broeke, and L Padman. “Antarctic ice-sheet loss driven by basal melting of ice shelves”. In: *Nature* 484 (Apr. 2012), pp. 502–5.
[19] L. Padman, M.R. Siegfried, and H.A. Fricker. “Ocean tide influences on the Antarctic and Greenland ice sheets”. In: *Reviews of Geophysics* 56 (2018), pp. 142–184.
[20] Laurie Padman, Matt King, Derek Goring, Hugh Corr, and Richard Coleman. “Ice-shelf elevation changes due to atmospheric pressure variations”. In: *Journal of Glaciology* 49.167 (2003), pp. 521–526.
[21] Anna E. Hogg, Lin Gilbert, Andrew Shepherd, Alan S. Muir, and Malcolm McMillan. “Extending the record of Antarctic ice shelf thickness change, from 1992 to 2017”. In: *Advances in Space Research* 68.2 (2021). 25 Years of Progress in Radar Altimetry, pp. 724–731.
[22] Weikang Sun, Xinghua Zhou, Dongxu Zhou, and Yanfei Sun. “Advances and Accuracy Assessment of Ocean Tide Models in the Antarctic Ocean”. In: *Frontiers in Earth Science* 10 (2022).
[23] Peter Friedl, Frank Weiser, Anke Fluhrer, and Matthias H. Braun. “Remote sensing of glacier and ice sheet grounding lines: A review”. In: *Earth-Science Reviews* 201 (2020), p. 102948.
[24] ESA. *Revisit and Coverage*. URL: https://sentinels.copernicus.eu/web/sentinel/user-guides/sentinel-1-sar/revisit-and-coverage.
[25] Charles Elachi and Jakob van Zyl. *Introduction to the Physics and Techniques of Remote Sensing*. John Wiley Sons, Inc., 2021.
[26] Alessandro Ferretti, Andrea Monti-Guarnieri, Claudio Prati, Fabio Rocca, and Didier Massonnet. *InSAR Principles: Guidelines for SAR Interferometry Processing and Interpretation. Part A. Interferometric SAR image processing and interpretation*. Ed. by Karen Fletcher. TM-19. ESTEC, Postbus 299, 2200 AG Noordwijk, The Netherlands: ESA Publications, Feb. 2007.
[27] URL: https://sentinels.copernicus.eu/web/sentinel/missions/sentinel-1/satellite-description/orbit.
[28] URL: https://www.esa.int/Enabling_Support/Space_Transportation/Types_of_orbits#SS0.
[29] Cataldo Guaragnella and Tiziana D’Orazio. “A Data-Driven Approach to SAR Data-Focusing”. In: *Sensors* 19.7 (2019).
[30] URL: https://hyp3-docs.asf.alaska.edu/guides/introduction_to_sar/.
[31] Africa Ixmucane Flores-Anderson, Kelsey E. Herndon, Emil Cherrington, Rajesh Thapa, Leah Kucera, Nguyen Hanh Guyen, Phoebe Odour, Anastasia Wahome, Karis Tenneson, Bako Mamane, David Saah, Farrukh Chishtie, and Ashutosh Limaye. *Introduction and Rationale*. Ed. by A. Flores, K. Herndon, R. Thapa, and E. Cherrington. NASA, 2019.
[32] Charles Elachi and Jakob van Zyl. *Introduction to the Physics and Techniques of Remote Sensing*. John Wiley Sons, Inc., 2021.
[33] Charles Elachi and Jakob van Zyl. *Introduction to the Physics and Techniques of Remote Sensing*. John Wiley Sons, Inc., 2021.
[34] ESA. *Types of orbits*. URL: https://www.esa.int/Enabling_Support/Space_Transportation/Types_of_orbits.
[35] NASA: NISAR MISSION. *Mission - Overview - Get to know SAR*. URL: https://nisar.jpl.nasa.gov/mission/get-to-know-sar/overview/.
[36] URL: https://sar.iceye.com/5.0/OverviewOfSAR/sarProcessing/.
[37] R. F. Hanssen. *Radar Interferometry: Data Interpretation and Error Analysis*. Vol. 2. Remote Sensing and Digital Image Processing. Dordrecht, The Netherlands: Kluwer Academic Publishers, 2001.
[38] Charles Elachi and Jakob van Zyl. *Introduction to the Physics and Techniques of Remote Sensing*. John Wiley Sons, Inc., 2021.
[39] Pascal Castellazzi and Wolfgang Schmid. “Ground displacements in the Lower Namoi region”. In: (2020).
[40] Alessandro Ferretti, Andrea Monti-Guarnieri, Claudio Prati, Fabio Rocca, and Didier Massonnet. *InSAR Principles: Guidelines for SAR Interferometry Processing and Interpretation. Part B. InSAR processing: a practical approach.* Ed. by Karen Fletcher. TM-19. ESTEC, Postbus 299, 2200 AG Noordwijk, The Netherlands: ESA Publications, Feb. 2007.
[41] NSIDC. *Ice sheets*. URL: https://nsidc.org/learn/parts-cryosphere/ice-sheets. (accessed 2024-02-12).

[42] E. Rignot, J. Mouginot, B. Scheuchl, and S. Jeong. “Changes in Antarctic Ice Sheet Motion Derived From Satellite Radar Interferometry Between 1995 and 2022”. In: *Geophysical research letters* 49 (2022).
[43] R. Bindschadler, H. Choi, A. Wichlacz, R. Bingham, J. Bohlander, K. Brunt, H. Corr, R. Drews, H. Fricker, M. Hall, R. Hindmarsh, J. Kohler, L. Padman, W. Rack, G. Rotschky, S. Urbini, P. Vornberger, and N. Young. “Getting around Antarctica: new high-resolution mappings of the grounded and freely-floating boundaries of the Antarctic ice sheet created for the International Polar Year”. In: *The Cryosphere* 5.3 (2011), pp. 569–588.
[44] Kenichi Matsuoka, Richard C.A. Hindmarsh, Geir Moholdt, Michael J. Bentley, Hamish D. Pritchard, Joel Brown, Howard Conway, Reinhard Drews, Gaël Durand, Daniel Goldberg, Tore Hattermann, Jonathan Kingslake, Jan T.M. Lenaerts, Carlos Martín, Robert Mulvaney, Keith W. Nicholls, Frank Pattyn, Neil Ross, Ted Scambos, and Pippa L. Whitehouse. “Antarctic ice rises and rumples: Their properties and significance for ice-sheet dynamics and evolution”. In: *Earth-Science Reviews* 150 (2015), pp. 724–745.
[45] Johannes Lohse. “Tidally induced ice dynamics at the calving front of Ekstroemisen, Antarctica, in the context of flow and fracture mechanics”. PhD thesis. Oct. 2012.
[46] Henner Sandhäger. “Quanitifizierung eisdynamischer und massenhaushaltsrelevanter Basisgrößen eines antarktischen Inlandeis-Schelfeis-Systems unter Einsatz eines numerischen Fließmodells.” PhD thesis. 2000.
[47] R. Porter-Smith, J. McKinlay, A. D. Fraser, and R. A. Massom. “Coastal complexity of the Antarctic continent”. In: *Earth System Science Data* 13.7 (2021), pp. 3103–3114.
[48] NSIDC. *Ice shelves*. URL: `https://nsidc.org/learn/parts-cryosphere/ice-shelves`. (accessed: 22.09.2023).
[49] Ted A. Scambos, Christina Hulbe, Mark Fahnestock, and Jennifer Bohlander. “The link between climate warming and break-up of ice shelves in the Antarctic Peninsula”. In: *Journal of Glaciology* 46.154 (2000), pp. 516–530.
[50] G. Hilmar Gudmundsson, Fernando S. Paolo, Susheel Adusumilli, and Helen A. Fricker. “Instantaneous Antarctic ice sheet mass loss driven by thinning ice shelves”. In: *Geophysical Research Letters* 46.23 (2019), pp. 13903–13909. eprint: `https://agupubs.onlinelibrary.wiley.com/doi/pdf/10.1029/2019GL085027`.
[51] K.A. Naughten, J. De Rydt, and S.H.R. et al. Rosier. “Two-timescale response of a large Antarctic ice shelf to climate change.” In: *Nat Commun 12* (2021).
[52] Fernando S. Paolo, Helen A. Fricker, and Laurie Padman. “Volume loss from Antarctic ice shelves is accelerating”. In: *Science* 348.6232 (2015), pp. 327–331. eprint: `https://www.science.org/doi/pdf/10.1126/science.aaa0940`.
[53] H.A. Fricker, Richard Coleman, Laurie Padman, Ted A. Scambos, Jennifer Bohlander, and Kelly M. Brunt. “Mapping the grounding zone of the Amery Ice Shelf, East Antarctica using InSAR, MODIS and ICESat”. In: *Antarctic Science* 21.5 (2009), pp. 515–532.
[54] C.T. Wild. “InSAR for tide modelling in Antarctic ice-shelf grounding zones”. PhD thesis. University of Canterbury, 2018.
[55] GCOS. URL: `https://gcos.wmo.int/en/essential-climate-variables/ice-sheets-ice-shelves`.
[56] Jonathan L. Bamber and Andres Rivera. “A review of remote sensing methods for glacier mass balance determination”. In: *Global and Planetary Change* 59.1 (2007). Mass Balance of Andean Glaciers, pp. 138–148.
[57] Robert H. Thomas. “The Dynamics of Marine Ice Sheets”. In: *Journal of Glaciology* 24.90 (1979), pp. 167–177.
[58] accessed:2024-06-01.
[59] H. Liu, K. C. Jezek, B. Li, and Z. Zhao. *Radarsat Antarctic Mapping Project Digital Elevation Model, Version 2*. `http://dx.doi.org/10.5067/8JKNEW6BFRVD`. Boulder, Colorado USA. NASA National Snow and Ice Data Center Distributed Active Archive Center. [2024-06-01]. 2015.
[60] Kenneth C. Jezek. “Glaciological properties of the Antarctic ice sheet from RADARSAT-1 synthetic aperture radar imagery”. In: *Annals of Glaciology* 29 (1999), pp. 286–290.
[61] E. Rignot, J. Mouginot, and B. Scheuchl. “MEaSUREs InSAR-Based Antarctica Ice Velocity Map, Version 2”. In: (2017).
[62] A. Humbert and D. Steinhage. “The evolution of the western rift area of the Fimbul Ice Shelf, Antarctica”. In: *The Cryosphere* 5.4 (2011), pp. 931–944.

[63] E. Rignot, J. Mouginot, and B. Scheuchl. “Ice Flow of the Antarctic Ice Sheet”. In: *Science* 333 (2011), pp. 1427–1430.
[64] J. Mouginot, B. Scheuchl, and E. Rignot. “Mapping of Ice Motion in Antarctica Using Synthetic-Aperture Radar Data”. In: *Remote Sensing* 4 (2012), pp. 2753–2767.
[65] R. Bindschadler, H. Choi, and ASAID Collaborators. *High-resolution Image-derived Grounding and Hydrostatic Lines for the Antarctic Ice Sheet*. Boulder, Colorado, USA: National Snow and Ice Data Center. Digital media. 2011.
[66] K. Matsuoka, A. Skoglund, and G. Roth. “Quantarctica: Simple Basemap from SCAR Antarctic Digital Database (ADD) Version 7.0.” In: *Norwegian Polar Institute* (2018).
[67] Ole Anders Nøst. “Measurements of ice thickness and seabed topography under the Fimbul Ice Shelf, Dronning Maud Land, Antarctica”. In: *Journal of Geophysical Research: Oceans* 109.C10 (2004). eprint: https://agupubs.onlinelibrary.wiley.com/doi/pdf/10.1029/2004JC002277.
[68] J. Lauber, T. Hattermann, L. de Steur, E. Darelius, and A. Fransson. “Hydrography and circulation below Fimbulisen Ice Shelf, East Antarctica, from 12 years of moored observations”. In: *EGUsphere* 2024 (2024), pp. 1–38.
[69] A. M. Le Brocq, A. J. Payne, and A. Vieli. “An Improved Antarctic Dataset for High Resolution Numerical Ice Sheet Models (ALBMAP v1)”. In: *Earth Syst. Sci. Data* 2 (2010), pp. 247–260.
[70] J. Mouginot, B. Scheuchl, and E. Rignot. *MEaSUREs Antarctic Boundaries for IPY 2007-2009 from Satellite Radar, Version 2*. Boulder, Colorado USA: NASA National Snow and Ice Data Center Distributed Active Archive Center. [Indicate subset used]. 2017.
[71] Yidongfang Si, Andrew L. Stewart, and Ian Eisenman. “Heat transport across the Antarctic Slope Front controlled by cross-slope salinity gradients”. In: *Science Advances* 9.18 (2023), eadd7049. eprint: https://www.science.org/doi/pdf/10.1126/sciadv.add7049.
[72] Andrew F. Thompson, Andrew L. Stewart, Paul Spence, and Karen J. Heywood. “The Antarctic Slope Current in a Changing Climate”. In: *Reviews of Geophysics* 56.4 (2018), pp. 741–770. eprint: https://agupubs.onlinelibrary.wiley.com/doi/pdf/10.1029/2018RG000624.
[73] Julius Lauber, Tore Hattermann, Laura de Steur, Elin Darelius, Matthis Auger, Ole Anders Nøst, and Geir Moholdt. “Warming beneath an East Antarctic ice shelf due to increased subpolar westerlies and reduced sea ice.” In: *Nature Geoscience* (2023).
[74] Katrin Lindbäck, Elin Darelius, and Geir Moholdt. “Basal melting and oceanic observations beneath Fimbulisen, East Antarctica.” In: *ESS Open Archive* (2023).
[75] URL: https://www.npolar.no/tone/.
[76] Ph.D. Bruce B. Parker. *Tidal Analysis and Prediction*. NOAA Special Publication NOS CO-OPS 3, 2007.
[77] B. I. D. Freer, O. J. Marsh, A. E. Hogg, H. A. Fricker, and L. Padman. “Modes of Antarctic tidal grounding line migration revealed by Ice, Cloud, and land Elevation Satellite-2 (ICESat-2) laser altimetry”. In: *The Cryosphere* 17.9 (2023), pp. 4079–4101.
[78] R. Sayag and M. Grae Worster. “Elastic dynamics and tidal migration of grounding lines modify subglacial lubrication and melting”. In: *Geophysical Research Letters* 40.22 (2013), pp. 5877–5881. eprint: https://agupubs.onlinelibrary.wiley.com/doi/pdf/10.1002/2013GL057942.
[79] Minyan Zhong, Mark Simons, Brent Minchew, and Lijun Zhu. “Inferring Tide-Induced Ephemeral Grounding in an Ice-Shelf-Stream System: Rutford Ice Stream, West Antarctica”. In: *Journal of Geophysical Research: Earth Surface* 128.2 (2023). e2022JF006789 2022JF006789, e2022JF006789. eprint: https://agupubs.onlinelibrary.wiley.com/doi/pdf/10.1029/2022JF006789.
[80] Jan Erik Arndt, Hans Werner Schenke, Martin Jakobsson, Frank O. Nitsche, Gwen Buys, Bruce Goleby, Michele Rebesco, Fernando Bohoyo, Jongkuk Hong, Jenny Black, Rudolf Greku, Gleb Udintsev, Felipe Barrios, Walter Reynoso-Peralta, Morishita Taisei, and Rochelle Wigley. “The International Bathymetric Chart of the Southern Ocean (IBCSO) Version 1.0—A new bathymetric compilation covering circum-Antarctic waters”. In: *Geophysical Research Letters* 40.12 (2013), pp. 3111–3117. eprint: https://agupubs.onlinelibrary.wiley.com/doi/pdf/10.1002/grl.50413.
[81] J.A. Griggs and J.L. Bamber. “Antarctic ice-shelf thickness from satellite radar altimetry”. In: *Journal of Glaciology* 57.203 (2011), pp. 485–498.
[82] Matt A. King, Nigel T. Penna, Peter J. Clarke, and Ed C. King. “Validation of ocean tide models around Antarctica using onshore GPS and gravity data”. In: *Journal of Geophysical Research: Solid Earth* 110.B8 (2005). eprint: https://agupubs.onlinelibrary.wiley.com/doi/pdf/10.1029/2004JB003390.

[83] E. Rignot, L. Padman, D. R. MacAyeal, and M. Schmeltz. “Observation of ocean tides below the Filchner and Ronne Ice Shelves, Antarctica, using synthetic aperture radar interferometry: Comparison with tide model predictions”. In: *Journal of Geophysical Research: Oceans* 105.C8 (2000), pp. 19615–19630. eprint: https://agupubs.onlinelibrary.wiley.com/doi/pdf/10.1029/1999JC000011.
[84] W. Rack, M. A. King, O. J. Marsh, C. T. Wild, and D. Floricioiu. “Analysis of ice shelf flexure and its InSAR representation in the grounding zone of the southern McMurdo Ice Shelf”. In: *The Cryosphere* 11.6 (2017), pp. 2481–2490.
[85] URL: https://earth.esa.int/eogateway/missions/terrasar-x-and-tandem-x.
[86] Anna Odh. “The tidal and atmospheric pressure influence on the vertical motion of the Fimbul ice shelf using DInSAR”. Unpublished manuscript. 2023.
[87] URL: https://sentinels.copernicus.eu/web/sentinel/user-guides/sentinel-1-sar/acquisition-modes/interferometric-wide-swath.
[88] *Sentinel-1 Bursts*. URL: https://asf.alaska.edu/datasets/daac/sentinel-1-bursts/.
[89] URL: https://sentinels.copernicus.eu/web/sentinel/user-guides/sentinel-1-sar/acquisition-modes/extra-wide-swath.
[90] Copernicus browser. *Sentinel-1 Satellite Imagery*. Accessed on: [2024-05-16]. 2024.
[91] Alessandro Ferretti, Andrea Monti-Guarnieri, Claudio Prati, Fabio Rocca, and Didier Massonnet. *InSAR Principles: Guidelines for SAR Interferometry Processing and Interpretation. InSAR processing: a mathematical approach*. Ed. by Karen Fletcher. TM-19. ESTEC, Postbus 299, 2200 AG Noordwijk, The Netherlands: ESA Publications, Feb. 2007.
[92] URL: https://www.esr.org/data-products/antarctic_tg_database/.
[93] URL: https://se.mathworks.com/matlabcentral/fileexchange/133417-tide-model-driver-tmd-version-3-0.
[94] URL: https://www.esr.org/research/polar-tide-models/list-of-polar-tide-models/cats2008/.
[95] Donghui Yi, Bernard Minster, and Charles Bentley. “The effect of ocean tidal loading on satellite altimetry over Antarctica”. In: *Antarctic Science* 12 (Mar. 2000).
[96] Jelte van Oostveen. Personal communication. 2024.
[97] J. Lauber, L. de Steur, T. Hattermann, and O.A. Nøst. *Daily averages of physical oceanography and current meter data from sub-ice-shelf moorings M1, M2 and M3 at Fimbulisen, East Antarctica since 2009*. Data set. 2023.
[98] *pyTMD*. URL: https://github.com/tsutterley/pyTMD.
[99] et al. Howat Ian. “The Reference Elevation Model of Antarctica – Mosaics, Version 2”. In: *Harvard Dataverse, V1* (2022).
[100] C. Werner, T. Strozzi, U. Wegmuller, and A. Wiesmann. “SAR geocoding and multi-sensor image registration”. In: 2 (2002), 902–904 vol.2.
[101] Jonathan M. Lilly and Peter B. Rhines. “Coherent Eddies in the Labrador Sea Observed from a Mooring”. In: *Journal of Physical Oceanography* 32.2 (2002), pp. 585–598.
[102] J. Martínez-Moreno, A. M. Hogg, M. H. England, and et al. “Global changes in oceanic mesoscale currents over the satellite altimetry record”. In: *Nature Climate Change* 11 (2021), pp. 397–403.
[103] Julius Lauber, Laura de Steur, Tore Hattermann, and et al. “Observed Seasonal Evolution of the Antarctic Slope Current System off the Coast of Dronning Maud Land, East Antarctica”. In: *ESS Open Archive* (Oct. 2023).
[104] URL: http://www.euro-cordex.be/meteo/view/en/29038090-MAR+model.html.